

Interrogating theoretical models of neural computation with deep inference
Sean R. Bittner¹, Agostina Palmigiano¹, Alex T. Piet^{2,3}, Chunyu A. Duan⁴, Carlos D. Brody^{2,3,5},
Kenneth D. Miller¹, and John P. Cunningham⁶.

¹Department of Neuroscience, Columbia University,

²Princeton Neuroscience Institute,

³Princeton University,

⁴Institute of Neuroscience, Chinese Academy of Sciences,

⁵Howard Hughes Medical Institute,

⁶Department of Statistics, Columbia University

¹ 1 Abstract

² A cornerstone of theoretical neuroscience is the circuit model: a system of equations that captures
³ a hypothesized neural mechanism. Such models are valuable when they give rise to an experimen-
⁴ tally observed phenomenon – whether behavioral or in terms of neural activity – and thus can
⁵ offer insights into neural computation. The operation of these circuits, like all models, critically
⁶ depends on the choices of model parameters. Historically, the gold standard has been to analyt-
⁷ ically derive the relationship between model parameters and computational properties. However,
⁸ this enterprise quickly becomes infeasible as biologically realistic constraints are included into the
⁹ model increasing its complexity, often resulting in *ad hoc* approaches to understanding the relation-
¹⁰ ship between model and computation. We bring recent machine learning techniques – the use of
¹¹ deep generative models for probabilistic inference – to bear on this problem, learning distributions
¹² of parameters that produce the specified properties of computation. Importantly, the techniques
¹³ we introduce offer a principled means to understand the implications of model parameter choices
¹⁴ on computational properties of interest. We motivate this methodology with a worked example
¹⁵ analyzing sensitivity in the stomatogastric ganglion. We then use it to go beyond linear theory
¹⁶ of neuron-type input-responsivity in a model of primary visual cortex, gain a mechanistic under-
¹⁷ standing of rapid task switching in superior colliculus models, and attribute error to connectivity
¹⁸ properties in recurrent neural networks solving a simple mathematical task. More generally, this
¹⁹ work suggests a departure from realism vs tractability considerations, towards the use of modern
²⁰ machine learning for sophisticated interrogation of biologically relevant models.

21 2 Introduction

22 The fundamental practice of theoretical neuroscience is to use a mathematical model to understand
23 neural computation, whether that computation enables perception, action, or some intermediate
24 processing [1]. A neural computation is systematized with a set of equations – the model – and
25 these equations are motivated by biophysics, neurophysiology, and other conceptual considerations.
26 The function of this system is governed by the choice of model parameters, which when configured
27 in a particular way, give rise to a measurable signature of a computation. The work of analyzing a
28 model then requires solving the inverse problem: given a computation of interest, how can we reason
29 about these particular parameter configurations? The inverse problem is crucial for reasoning about
30 likely parameter values, uniquenesses and degeneracies, attractor states and phase transitions, and
31 predictions made by the model.

32 Consider the idealized practice: one carefully designs a model and analytically derives how model
33 parameters govern the computation. Seminal examples of this gold standard (which often adopt
34 approaches from statistical physics) include our field’s understanding of memory capacity in asso-
35 ciative neural networks [2], chaos and autocorrelation timescales in random neural networks [3],
36 the paradoxical effect [4], and decision making [5]. Unfortunately, as circuit models include more
37 biological realism, theory via analytical derivation becomes intractable. This creates an unfavor-
38 able tradeoff. On the one hand, one may tractably analyze systems of equations with unrealistic
39 assumptions (for example symmetry or gaussianity), mathematically formalizing how parameters
40 affect computation in a too-simple model. On the other hand, one may choose a more biologically
41 accurate, scientifically relevant model at the cost of *ad hoc* approaches to analysis (such as sim-
42 ply examining simulated activity), potentially resulting in bad inference of parameters and thus
43 erroneous scientific predictions or conclusions.

44 Of course, this same tradeoff has been confronted in many scientific fields characterized by the
45 need to do inference in complex models. In response, the machine learning community has made
46 remarkable progress in recent years, via the use of deep neural networks as a powerful inference
47 engine: a flexible function family that can map observed phenomena (in this case the measurable
48 signal of some computation) back to probability distributions quantifying the likely parameter
49 configurations. One celebrated example of this approach from machine learning, of which we
50 draw key inspiration for this work, is the variational autoencoder [6, 7], which uses a deep neural
51 network to induce an (approximate) posterior distribution on hidden variables in a latent variable

model, given data. Indeed, these tools have been used to great success in neuroscience as well, in particular for interrogating parameters (sometimes treated as hidden states) in models of both cortical population activity [8, 9, 10, 11] and animal behavior [12, 13, 14]. These works have used deep neural networks to expand the expressivity and accuracy of statistical models of neural data [15].

However, these inference tools have not significantly influenced the study of theoretical neuroscience models, for at least three reasons. First, at a practical level, the nonlinearities and dynamics of many theoretical models are such that conventional inference tools typically produce a narrow set of insights into these models. Indeed, only in the last few years has deep learning research advanced to a point of relevance to this class of problem. Second, the object of interest from a theoretical model is not typically data itself, but rather a qualitative phenomenon – inspection of model behavior, or better, a measurable signature of some computation – an *emergent property* of the model. Third, because theoreticians work carefully to construct a model that has biological relevance, such a model as a result often does not fit cleanly into the framing of a statistical model. Technically, because many such models stipulate a noisy system of differential equations that can only be sampled or realized through forward simulation, they lack the explicit likelihood and priors central to the probabilistic modeling toolkit.

To address these three challenges, we developed an inference methodology – ‘emergent property inference’ – which learns a distribution over parameter configurations in a theoretical model. This distribution has two critical properties: (*i*) it is chosen such that draws from the distribution (parameter configurations) correspond to systems of equations that give rise to a specified emergent property (a set of constraints); and (*ii*) it is chosen to have maximum entropy given those constraints, such that we identify all likely parameters and can use the distribution to reason about parametric sensitivity and degeneracies [16]. First, we stipulate a bijective deep neural network that induces a flexible family of probability distributions over model parameterizations with a probability density we can calculate [17, 18, 19]. Second, we quantify the notion of emergent properties as a set of moment constraints on datasets generated by the model. Thus, an emergent property is not a single data realization, but a phenomenon or a feature of the model, which is ultimately the object of interest in theoretical neuroscience. Conditioning on an emergent property requires a variant of deep probabilistic inference methods, which we have previously introduced [20]. Third, because we cannot assume the theoretical model has explicit likelihood on data or the emergent property of interest, we use stochastic gradient techniques in the spirit of likelihood free variational inference

[21]. Taken together, emergent property inference (EPI) provides a methodology for inferring parameter configurations consistent with a particular emergent phenomena in theoretical models. We use a classic example of parametric degeneracy in a biological system, the stomatogastric ganglion [22], to motivate and clarify the technical details of EPI.

Equipped with this methodology, we then investigated three models of current importance in theoretical neuroscience. These models were chosen to demonstrate generality through ranges of biological realism (from conductance-based biophysics to recurrent neural networks), neural system function (from pattern generation to abstract cognitive function), and network scale (from four to infinite neurons). First, we use EPI to produce a set of verifiable hypotheses of input-responsivity in a four neuron-type dynamical model of primary visual cortex; we then validate these hypotheses in the model. Second, we demonstrated how the systematic application of EPI to levels of task performance can generate experimentally testable hypotheses regarding connectivity in superior colliculus. Third, we use EPI to uncover the sources of error in a low-rank recurrent neural network executing a simple mathematical task. The novel scientific insights offered by EPI contextualize and clarify the previous studies exploring these models [23, 24, 25, 26], and more generally, these results point to the value of deep inference for the interrogation of biologically relevant models.

We note that, during our preparation and early presentation of this work [27, 28], another work has arisen with broadly similar goals: bringing statistical inference to mechanistic models of neural circuits [29, 30]. We are encouraged by this general problem being recognized by others in the community, and we emphasize that these works offer complementary neuroscientific contributions (different theoretical models of focus) and use different technical methodologies (ours is built on our prior work [20], theirs similarly [31]). These distinct methodologies and scientific investigations emphasize the increased importance and timeliness of both works.

3 Results

3.1 Motivating emergent property inference of theoretical models

Consideration of the typical workflow of theoretical modeling clarifies the need for emergent property inference. First, one designs or chooses an existing model that, it is hypothesized, captures the computation of interest. To ground this process in a well-known example, consider the stomatogastric ganglion (STG) of crustaceans, a small neural circuit which generates multiple rhythmic muscle activation patterns for digestion [32]. Despite full knowledge of STG connectivity and a

114 precise characterization of its rhythmic pattern generation, biophysical models of the STG have
 115 complicated relationships between circuit parameters and neural activity [22, 33]. A model of the
 116 STG [23] is shown schematically in Figure 1A, and note that the behavior of this model will be crit-
 117 ically dependent on its parameterization – the choices of conductance parameters $z = [g_{el}, g_{synA}]$.
 118 Specifically, the two fast neurons (f_1 and f_2) mutually inhibit one another, and oscillate at a faster
 119 frequency than the mutually inhibiting slow neurons (s_1 and s_2). The hub neuron (hub) couples
 120 with either the fast or slow population or both.
 121 Second, once the model is selected, one defines the emergent property, the measurable signal of
 122 scientific interest. To continue our running STG example, one such emergent property is the
 123 phenomenon of *network syncing* – in certain parameter regimes, the frequency of the hub neuron
 124 matches that of the fast and slow populations at an intermediate frequency. This emergent property
 125 is shown in Figure 1A at a frequency of 0.53Hz.
 126 Third, qualitative parameter analysis ensues: since precise mathematical analysis is intractable in
 127 this model, a brute force sweep of parameters is done [23]. Subsequently, a qualitative description
 128 is formulated to describe the different parameter configurations that lead to the emergent property.
 129 In this last step lies the opportunity for a precise quantification of the emergent property as a
 130 statistical feature of the model. Once we have such a methodology, we can infer a probability
 131 distribution over parameter configurations that produce this emergent property.
 132 Before presenting technical details (in the following section), let us understand emergent property
 133 inference schematically: EPI (Fig. 1A gray box) takes, as input, the model and the specified
 134 emergent property, and as its output, produces the parameter distribution shown in Figure 1B.
 135 This distribution – represented for clarity as samples from the distribution – is then a scientifically
 136 meaningful and mathematically tractable object. In the STG model, this distribution can be
 137 specifically queried to reveal the prototypical parameter configuration for network syncing (the
 138 mode; Figure 1B yellow star), and how network syncing decays based on changes away from the
 139 mode. The eigenvectors (of the Hessian of the distribution at the mode) quantitatively formalize
 140 the robustness of network syncing (Fig. 1B solid (v_1) and dashed (v_2) black arrows). Indeed,
 141 samples equidistant from the mode along these EPI-identified dimensions of sensitivity (v_1) and
 142 degeneracy (v_2) agree with error contours (Fig. 1B, contours) and have diminished or preserved
 143 network syncing, respectively (Figure 1B inset and activity traces) (see Section B.2.1).

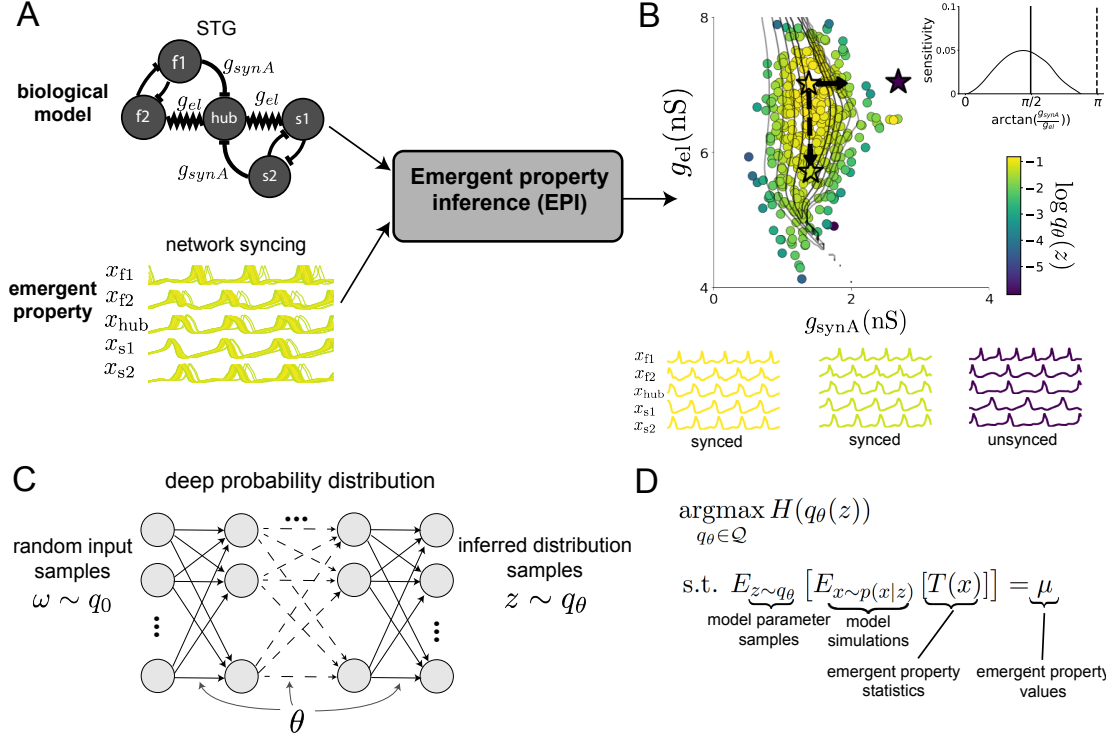


Figure 1: Emergent property inference (EPI) in the stomatogastric ganglion. A. For a choice of model (STG) and emergent property (network syncing), emergent property inference (EPI, gray box) learns a distribution of the model parameters $z = [g_{el}, g_{synA}]$ producing network syncing. In the STG model, jagged connections indicate electrical coupling having electrical conductance g_{el} . Other connections in the diagram are inhibitory synaptic projections having strength g_{synA} onto the hub neuron, and $g_{synB} = 5\text{nS}$ for mutual inhibitory connections. Network syncing traces are colored by log probability density of their generating parameters (stars) in the EPI-inferred distribution. B. The EPI distribution of STG model parameters producing network syncing. Samples are colored by log probability density. Distribution contours of emergent property value error are shown at levels of 2.5×10^{-5} , 5×10^{-5} , 1×10^{-4} , 2×10^{-4} , and 4×10^{-4} (dark to light gray). Eigenvectors of the Hessian at the mode of the inferred distribution are indicated as v_1 (solid) and v_2 (dashed) with lengths scaled by the square root of the absolute value of their eigenvalues. Simulated activity is shown for three samples (stars). (Inset) Sensitivity of the system with respect to network syncing along all dimensions of parameter space away from the mode. v_1 is sensitive to network syncing ($p < 10^{-4}$), while v_2 is not ($p = 0.67$) (see Section B.2.1). C. Deep probability distributions map a latent random variable w through a deep neural network with weights and biases θ to parameters $z = f_\theta(w)$ distributed as $q_\theta(z)$. D. EPI optimization: To learn the EPI distribution $q_\theta(z)$ of model parameters that produce an emergent property, the emergent property statistics $T(x)$ are set in expectation over model parameter samples $z \sim q_\theta(z)$ and model simulations $x \sim p(x | z)$ to emergent property values μ .

144 3.2 A deep generative modeling approach to emergent property inference

145 Emergent property inference (EPI) systematizes the three-step procedure of the previous section.
 146 First, we consider the model as a coupled set of differential (and potentially stochastic) equations
 147 [23]. In the running STG example, the model activity $x = [x_{f1}, x_{f2}, x_{hub}, x_{s1}, x_{s2}]$ is the membrane
 148 potential for each neuron, which evolves according to the biophysical conductance-based equation:

$$C_m \frac{dx}{dt} = -h(x; z) = -[h_{leak}(x; z) + h_{Ca}(x; z) + h_K(x; z) + h_{hyp}(x; z) + h_{elec}(x; z) + h_{syn}(x; z)] \quad (1)$$

149 where $C_m = 1\text{nF}$, and h_{leak} , h_{Ca} , h_K , h_{hyp} , h_{elec} , and h_{syn} are the leak, calcium, potassium, hyper-
 150 polarization, electrical, and synaptic currents, all of which have their own complicated dependence
 151 on x and $z = [g_{el}, g_{synA}]$ (see Section B.2.1).

152 Second, we define the emergent property, which as above is network syncing: oscillation of the
 153 entire population at an intermediate frequency of our choosing (Figure 1A bottom). Quantifying
 154 this phenomenon is straightforward: we define network syncing to be that each neuron’s spiking
 155 frequency – denoted $\omega_{f1}(x)$, $\omega_{f2}(x)$, etc. – is close to an intermediate frequency of 0.53Hz. Math-
 156 ematically, we achieve this via constraints on the mean and variance of $\omega_\alpha(x)$ for each neuron
 157 $\alpha \in \{f1, f2, hub, s1, s2\}$:

$$\mathbb{E}[T(x)] \triangleq \mathbb{E} \begin{bmatrix} \omega_{f1}(x) \\ \vdots \\ (\omega_{f1}(x) - 0.53)^2 \\ \vdots \end{bmatrix} = \begin{bmatrix} 0.53 \\ \vdots \\ 0.025^2 \\ \vdots \end{bmatrix} \triangleq \mu, \quad (2)$$

158 which completes the quantification of the emergent property.

159 Third, we perform emergent property inference: we find a distribution over parameter configura-
 160 tions z , and insist that samples from this distribution produce the emergent property; in other
 161 words, they obey the constraints introduced in Equation 2. This distribution will be chosen from
 162 a family of probability distributions $\mathcal{Q} = \{q_\theta(z) : \theta \in \Theta\}$, defined by a deep generative distribution
 163 of the normalizing flow class [17, 18, 19] – neural networks which transform a simple distribution
 164 into a suitably complicated distribution (as is needed here). This deep distribution is represented
 165 in Figure 1C (see Section B.1). Then, mathematically, we must solve the following optimization
 166 program:

$$\begin{aligned} & \underset{q_\theta \in \mathcal{Q}}{\operatorname{argmax}} H(q_\theta(z)) \\ & \text{s.t. } \mathbb{E}_{z \sim q_\theta} [\mathbb{E}_{x \sim p(x|z)} [T(x)]] = \mu, \end{aligned} \quad (3)$$

where $T(x), \mu$ are defined as in Equation 2, and $p(x|z)$ is the intractable distribution of data from the model, x , given that model's parameters z (we access samples from this distribution by running the model forward). The purpose of each element in this program is detailed in Figure 1D. Finally, we recognize that many distributions in \mathcal{Q} will respect the emergent property constraints, so we require a normative principle to select amongst them. This principle is captured in Equation 3 by the primal objective H . Here we chose Shannon entropy as a means to find parameter distributions with minimal assumptions beyond some chosen structure [34, 35, 20, 36], but we emphasize that the EPI methodology is unaffected by this choice (although the results of course depend on the primal objective chosen).

EPI optimizes the weights and biases θ of the deep neural network (which induces the probability distribution) by iteratively solving Equation 3. The optimization is complete when the sampled models with parameters $z \sim q_\theta$ produce activity consistent with the specified emergent property (Fig. S4). Such convergence is evaluated with a hypothesis test that the mean of each emergent property statistic is not different than its emergent property value (see Section B.1.2). Further validation of EPI is available in the supplementary materials, where we analyze a simpler model for which ground-truth statements can be made (Section B.1.1). In relation to broader methodology, inspection of the EPI objective reveals a natural relationship to posterior inference. Specifically, EPI executes variational inference in an exponential family model, the sufficient statistics and mean parameter of which are defined by the emergent property statistics and values, respectively (see Section B.1.4). Equipped with this method, we now prove out the value of EPI by using it to investigate and produce novel insights about three prominent models in neuroscience.

3.3 Comprehensive input-responsivity in a nonlinear sensory system

Dynamical models of excitatory (E) and inhibitory (I) populations with supralinear input-output function have succeeded in explaining a host of experimentally documented phenomena. In a regime characterized by inhibitory stabilization of strong recurrent excitation, these models give rise to paradoxical responses [4], selective amplification [37], surround suppression [38] and normalization [39]. Despite their strong predictive power, E-I circuit models rely on the assumption that inhibition can be studied as an indivisible unit. However, experimental evidence shows that inhibition is composed of distinct elements – parvalbumin (P), somatostatin (S), VIP (V) – composing 80% of GABAergic interneurons in V1 [40, 41, 42], and that these inhibitory cell types follow specific connectivity patterns (Fig. 2A) [43]. Recent theoretical advances [24, 44, 45], have only started

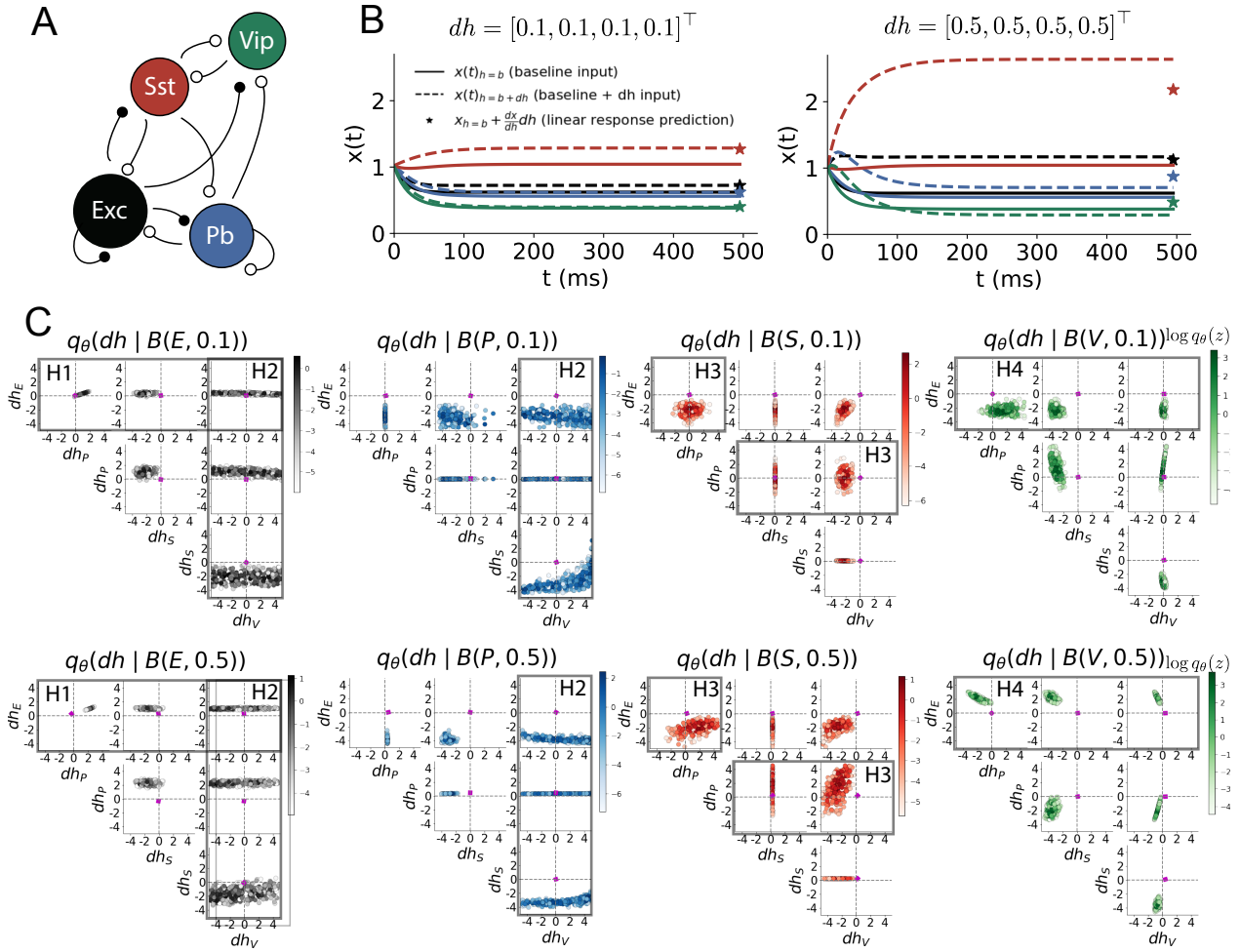


Figure 2: Hypothesis generation through EPI in a V1 model. A. Four-population model of primary visual cortex with excitatory (black), parvalbumin (blue), somatostatin (red), and VIP (green) neurons. Some neuron-types largely do not form synaptic projections to others (excitatory and inhibitory projections filled and unfilled, respectively). B. Linear response predictions become inaccurate with greater input strength. V1 model simulations for input (solid) $h = b$ and (dashed) $h = b + dh$. Stars indicate the linear response prediction. C. EPI distributions on differential input dh conditioned on differential response $\mathcal{B}(\alpha, y)$. Supporting evidence for the four generated hypotheses are indicated by gray boxes with labels H1, H2, H3, and H4. The linear prediction from two standard deviations away from y (from negative to positive) is overlaid in magenta (very small, near origin).

198 to address the consequences of this multiplicity in the dynamics of V1, strongly relying on linear
 199 theoretical tools. Here, we go beyond linear theory by systematically generating and evaluating hy-
 200 potheses of circuit model function using EPI distributions of neuron-type inputs producing various
 201 neuron-type population responses.

202 Specifically, we consider a four-dimensional circuit model with dynamical state given by the firing
 203 rate x of each neuron-type population $x = [x_E, x_P, x_S, x_V]^\top$. Given a time constant of $\tau = 20$ ms
 204 and a power $n = 2$, the dynamics are driven by the rectified and exponentiated sum of recurrent
 205 (Wx) and external h inputs:

$$\tau \frac{dx}{dt} = -x + [Wx + h]_+^n. \quad (4)$$

206 The effective connectivity weights W were obtained from experimental recordings of publicly avail-
 207 able datasets of mouse V1 [46, 47] (see Section B.2.2). The input $h = b + dh$ is comprised of a
 208 baseline input $b = [b_E, b_P, b_S, b_V]^\top$ and a differential input $dh = [dh_E, dh_P, dh_S, dh_V]^\top$ to each
 209 neuron-type population. Throughout subsequent analyses, the baseline input is $b = [1, 1, 1, 1]^\top$.

210 With this model, we are interested in the differential responses of each neuron-type population to
 211 changes in input dh . Initially, we studied the linearized response of the system to input $\frac{dx_{ss}}{dh}$ at the
 212 steady state response x_{ss} , i.e. a fixed point. All analyses of this model consider the steady state
 213 response, so we drop the notation ss from here on. While this linearization accurately predicts
 214 differential responses $dx = [dx_E, dx_P, dx_S, dx_V]^\top$ for small differential inputs to each population
 215 $dh = [0.1, 0.1, 0.1, 0.1]^\top$ (Fig 2B left), the linearization is a poor predictor in this nonlinear model
 216 more generally (Fig. 2B right). Currently available approaches to deriving the steady state response
 217 of the system are limited.

218 To get a more comprehensive picture of the input-responsivity of each neuron-type beyond linear
 219 theory, we used EPI to learn a distribution of the differential inputs to each population dh that
 220 produce an increase of y in the rate of each neuron-type population $\alpha \in \{E, P, S, V\}$. We want
 221 to know the differential inputs dh that result in a differential steady state dx_α (the change in x_α
 222 when receiving input $h = b + dh$ with respect to the baseline $h = b$) of value y with some small,
 223 arbitrarily chosen amount of variance 0.01^2 . These statements amount to the emergent property

$$\mathcal{B}(\alpha, y) \triangleq \mathbb{E} \begin{bmatrix} dx_\alpha \\ (dx_\alpha - y)^2 \end{bmatrix} = \begin{bmatrix} y \\ 0.01^2 \end{bmatrix}. \quad (5)$$

224 We maintain the notation $\mathcal{B}(\cdot)$ throughout the rest of the study as short hand for emergent property,

which represents a different signature of computation in each application.

Using EPI, we inferred the distribution of dh shown in Figure 2C producing $\mathcal{B}(\alpha, y)$. Columns correspond to inferred distributions of excitatory ($\alpha = E$, red), parvalbumin ($\alpha = P$, blue), somatostatin ($\alpha = S$, red) and VIP ($\alpha = V$, green) neuron-type response increases, while each row corresponds to increase amounts of $y \in \{0.1, 0.5\}$. For each pair of parameters, we show the two-dimensional marginal distribution of samples colored by $\log q_\theta(dh | \mathcal{B}(\alpha, y))$. The inferred distributions immediately suggest four hypotheses:

232

- 233 H1: as is intuitive, each neuron-type's firing rate should be sensitive to that neuron-type's
234 direct input (e.g. Fig. 2C H1 gray boxes indicate low variance in dh_E when $\alpha = E$. Same
235 observation in all inferred distributions);
 - 236 H2: the E- and P-populations should be largely unaffected by input to the V-population (Fig.
237 2C H2 gray boxes indicate high variance in dh_V when $\alpha \in \{E, P\}$);
 - 238 H3: the S-population should be largely unaffected by input to the P-population (Fig. 2C H3
239 gray boxes indicate high variance in dh_P when $\alpha = S$);
 - 240 H4: there should be a nonmonotonic response of the V-population with input to the E-
241 population (Fig. 2C H4 gray boxes indicate that negative dh_E should result in small dx_V ,
242 but positive dh_E should elicit a larger dx_V);
- 243 We evaluate these hypotheses by taking perturbations in individual neuron-type input δh_α away
244 from the modes of the inferred distributions at $y = 0.1$

$$dh^* = z^* = \underset{z}{\operatorname{argmax}} \log q_\theta(z | \mathcal{B}(\alpha, 0.1)). \quad (6)$$

245 Here δx_α is the change in steady state response of the system with input $h = b + dh^* + \delta h_\alpha \hat{u}_\alpha$
246 compared to $h = b + dh^*$, where \hat{u}_α is a unit vector in the dimension of α . The EPI-generated
247 hypotheses are confirmed (for details, see Section B.2.2):

- 248 H1: the neuron-type responses are sensitive to their direct inputs (Fig. 3A black, 3B blue,
249 3C red, 3D green);
- 250 H2: the E- and P-populations are not affected by δh_V (Fig. 3A green, 3B green);
- 251 H3: the S-population is not affected by δh_P (Fig. 3C blue);
- 252 H4: the V-population exhibits a nonmonotonic response to δh_E (Fig. 3D black), and is in
253 fact the only population to do so (Fig. 3A-C black).

254 These hypotheses were in stark contrast to what was available to us via traditional analytical

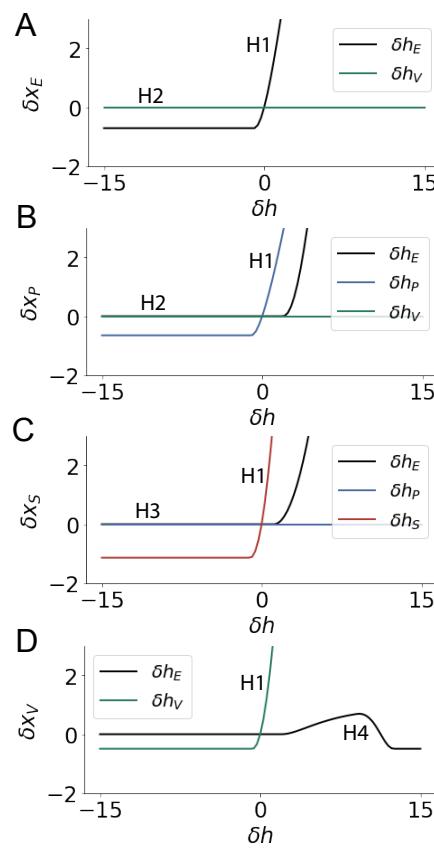


Figure 3: Confirming EPI generated hypotheses in V1. A. Differential responses δx_E by the E-population to changes in individual input $\delta h_\alpha \hat{u}_\alpha$ away from the mode of the EPI distribution dh^* . B-D Same plots for the P-, S-, and V-populations. Labels H1, H2, H3, and H4 indicate which curves confirm which hypotheses.

255 linear prediction (Fig. 2C, magenta, see Section B.2.2). To this point, we have shown the utility of
 256 EPI on relatively low-level emergent properties like network syncing and differential neuron-type
 257 population responses. In the remainder of the study, we focus on using EPI to understand models
 258 of more abstract cognitive function.

259 3.4 Identifying neural mechanisms of flexible task switching

260 In a rapid task switching experiment [48], rats were explicitly cued on each trial to either orient
 261 towards a visual stimulus in the Pro (P) task or orient away from a visual stimulus in the Anti
 262 (A) task (Fig. 4a). Neural recordings in the midbrain superior colliculus (SC) exhibited two
 263 populations of neurons that simultaneously represented both task context (Pro or Anti) and motor
 264 response (contralateral or ipsilateral to the recorded side): the Pro/Contra and Anti/Ipsi neurons
 265 [25]. Duan et al. proposed a model of SC that, like the V1 model analyzed in the previous section, is
 266 a four-population dynamical system. We analyzed this model, where the neuron-type populations
 267 are functionally-defined as the Pro- and Anti-populations in each hemisphere (left (L) and right
 268 (R)), their connectivity is parameterized geometrically (Fig. 4B). The input-output function of
 269 this model is chosen such that the population responses $x = [x_{LP}, x_{LA}, x_{RP}, x_{RA}]^\top$ are bounded

270 from 0 to 1 giving rise to high (1) or low (0) responses at the end of the trial:

$$x_\alpha = \left(\frac{1}{2} \tanh \left(\frac{u_\alpha - \epsilon}{\zeta} \right) + \frac{1}{2} \right) \quad (7)$$

271 where $\epsilon = 0.05$ and $\zeta = 0.5$. The dynamics evolve with timescale $\tau = 0.09$ via an internal variable
272 u governed by connectivity weights W

$$\tau \frac{du}{dt} = -u + Wx + h + \sigma dB \quad (8)$$

273 with gaussian noise of variance $\sigma^2 = 1$. The input h is comprised of a cue-dependent input to the
274 Pro or Anti populations, a stimulus orientation input to either the Left or Right populations, and
275 a choice-period input to the entire network (see Section B.2.3). Here, we use EPI to determine the
276 changes in network connectivity $z = [sW_P, sW_A, vW_{PA}, vW_{AP}, dW_{PA}, dW_{AP}, hW_P, hW_A]$ resulting
277 in greater levels of rapid task switching accuracy.

278 To quantify the emergent property of rapid task switching at various levels of accuracy, we consid-
279 ered the requirements of this model in this behavioral paradigm. At the end of successful trials,
280 the response of the Pro population in the hemisphere of the correct choice must have a value near
281 1, while the Pro population in the opposite hemisphere must have a value near 0. Constraining a
282 population response $x_\alpha \in [0, 1]$ to be either 0 or 1 can be achieved by requiring that it has Bernoulli
283 variance (see Section B.2.3). Thus, we can formulate rapid task switching at a level of accuracy
284 $p \in [0, 1]$ in both tasks in terms of the average steady response of the Pro population \hat{p} of the
285 correct choice, the error in Bernoulli variance of that Pro neuron σ_{err}^2 , and the average difference
286 in Pro neuron responses d in both Pro and Anti trials:

$$\mathcal{B}(p) \triangleq \mathbb{E} \begin{bmatrix} \hat{p}_P \\ \hat{p}_A \\ (\hat{p}_P - p)^2 \\ (\hat{p}_A - p)^2 \\ \sigma_{P,err}^2 \\ \sigma_{A,err}^2 \\ d_P \\ d_A \end{bmatrix} = \begin{bmatrix} p \\ p \\ 0.15^2 \\ 0.15^2 \\ 0 \\ 0 \\ 1 \\ 1 \end{bmatrix}. \quad (9)$$

287 Thus, $\mathcal{B}(p)$ denotes Bernoulli, winner-take-all responses between Pro neurons in a model executing
288 rapid task switching near accuracy level p .

289 We used EPI to learn distributions of the SC weight matrix parameters z conditioned on of various
290 levels of rapid task switching accuracy $\mathcal{B}(p)$ for $p \in \{50\%, 60\%, 70\%, 80\%, 90\%\}$. To make sense

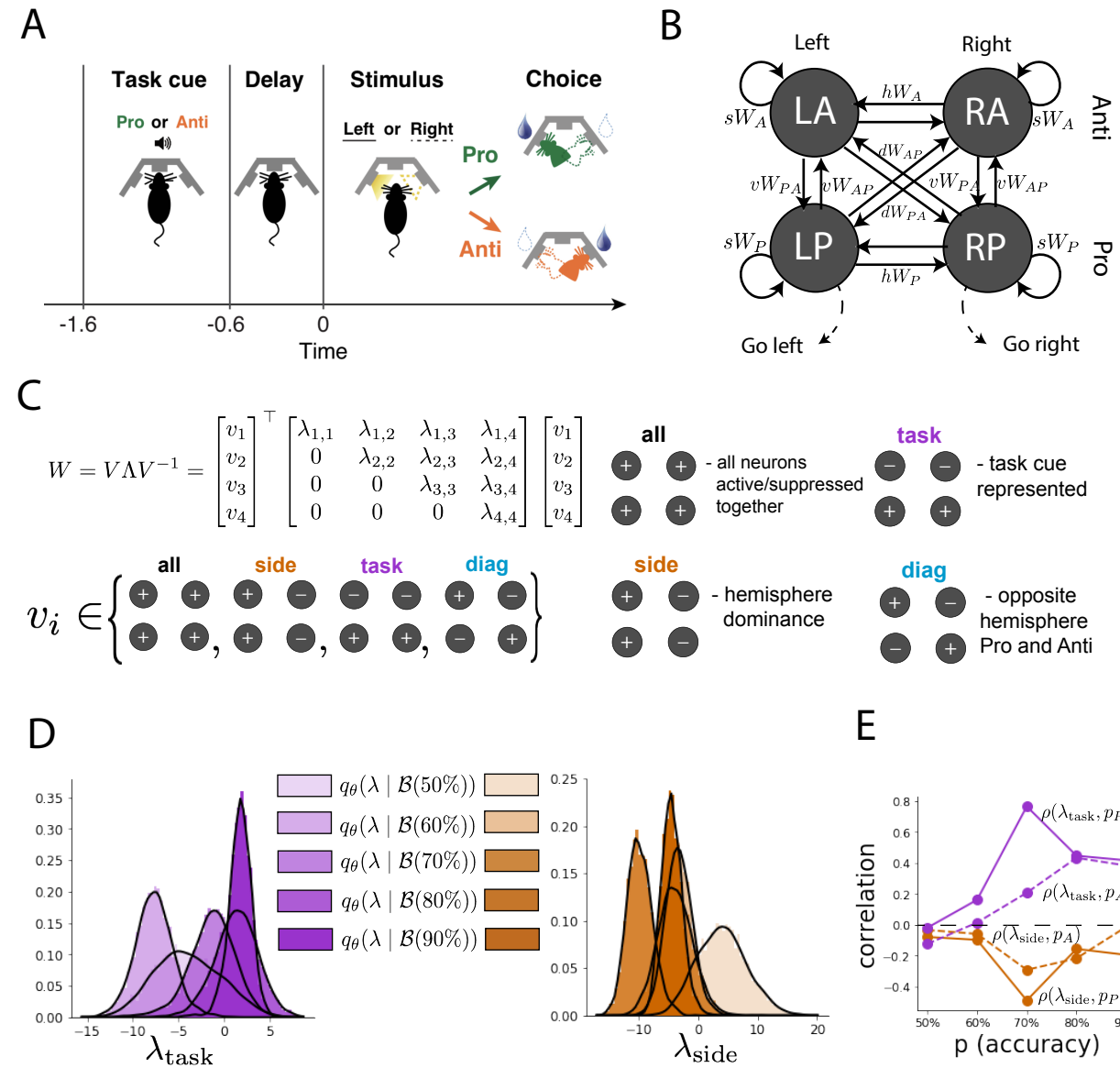


Figure 4: EPI reveals changes in SC [25] connectivity that control task accuracy. A. Rapid task switching behavioral paradigm (see text). B. Model of superior colliculus (SC). Neurons: LP - left pro, RP - right pro, LA - left anti, RA - right anti. Parameters: sW - self, hW - horizontal, vW - vertical, dW - diagonal weights. Subscripts P and A of connectivity weights indicate Pro or Anti populations, and e.g. vW_{PA} is a vertical weight from an Anti to a Pro population. C. The Schur decomposition of the weight matrix $W = V \Lambda V^{-1}$ is a unique decomposition with orthogonal V and upper triangular Λ . Schur modes: v_{all} , v_{task} , v_{side} , and v_{diag} . D. The marginal EPI distributions of the Schur eigenvalues at each level of task accuracy. E. The correlation of Schur eigenvalue with task performance in each learned EPI distribution.

of these inferred distributions, we followed the approach of Duan et al. by decomposing the connectivity matrix $W = V\Lambda V^{-1}$ in such a way (the Schur decomposition) that the basis vectors v_i are the same for all W (Fig. 4C). These basis vectors have intuitive roles in processing for this task, and are accordingly named the *all* mode - all neurons co-fluctuate, *side* mode - one side dominates the other, *task* mode - the Pro or Anti populations dominate the other, and *diag* mode - Pro- and Anti-populations of opposite hemispheres dominate the opposite pair. The corresponding eigenvalues (e.g. λ_{task} , which change according to W) indicate the degree to which activity along that mode is increased or decreased by W .

We found that for greater task accuracies, the task mode eigenvalue increases, indicating the importance of W to the task representation (Fig. 4D, purple; adjacent distributions from 60% to 90% have $p < 10^{-4}$, Mann-Whitney test with 50 estimates and 100 samples). Stepping from random chance (50%) networks to marginally task-performing (60%) networks, there is a marked decrease of the side mode eigenvalues (Fig. 4D, orange; $p < 10^{-4}$). Such side mode suppression relative to 50% remains in the models achieving greater accuracy, revealing its importance towards task performance. There were no interesting trends with task accuracy in the all or diag mode (hence not shown in Fig. 4). Importantly, we can conclude from our methodology that side mode suppression in W allows rapid task switching, and that greater task-mode representations in W increase accuracy. These hypotheses are confirmed by forward simulation of the SC model (Fig. 4E, see Section B.2.3) suggesting experimentally testable predictions: increase in rapid task switching performance should be correlated with changes in effective connectivity corresponding to an increase in task mode and decrease in side mode eigenvalues.

3.5 Linking RNN connectivity to error

So far, each model we have studied was designed from fundamental biophysical principles, genetically- or functionally-defined neuron types. At a more abstract level of modeling, recurrent neural networks (RNNs) are high-dimensional dynamical models of computation that are becoming increasingly popular in neuroscience research [49]. In theoretical neuroscience, RNN dynamics usually follow the equation

$$\frac{dx}{dt} = -x + W\phi(x) + h, \quad (10)$$

where x is the network activity, W is the network connectivity, $\phi(\cdot) = \tanh(\cdot)$, and h is the input to the system. Such RNNs are trained to do a task from a systems neuroscience experiment, and then the unit activations of the trained RNN are compared to recorded neural activity. Fully-connected

321 RNNs with tens of thousands of parameters are challenging to characterize [50], especially making
 322 statistical inferences about their parameterization. Alternatively, we considered a rank-1, N -neuron
 323 RNN with connectivity consisting of the sum of a random and a structured component:

$$W = g\chi + \frac{1}{N}mn^\top. \quad (11)$$

324 The random component $g\chi$ has strength g , and random component weights are Gaussian dis-
 325 tributed $\chi_{i,j} \sim \mathcal{N}(0, \frac{1}{N})$. The structured component $\frac{1}{N}mn^\top$ has entries of m and n drawn from
 326 Gaussian distributions $m_i \sim \mathcal{N}(M_m, 1)$ and $n_i \sim \mathcal{N}(M_n, 1)$. Recent theoretical work derives the
 327 low-dimensional response properties of low-rank networks from statistical parameterizations of their
 328 connectivity, such as $z = [g, M_m, M_n]$ [26]. We used EPI to infer the parameterizations of rank-
 329 1 RNNs solving an example task, enabling discovery of properties of connectivity that result in
 330 different types of error in the computation.

331 The task we consider is Gaussian posterior conditioning: calculate the parameters of a posterior
 332 distribution induced by a prior $p(\mu_y) = \mathcal{N}(\mu_0 = 4, \sigma_0^2 = 1)$ and a likelihood $p(y|\mu_y) = \mathcal{N}(\mu_y, \sigma_y^2 =$
 333 1), given a single observation y . Conjugacy offers the result analytically; $p(\mu_y|y) = \mathcal{N}(\mu_{post}, \sigma_{post}^2)$,

334 where:

$$\mu_{post} = \frac{\frac{\mu_0}{\sigma_0^2} + \frac{y}{\sigma_y^2}}{\frac{1}{\sigma_0^2} + \frac{1}{\sigma_y^2}} \quad \sigma_{post}^2 = \frac{1}{\frac{1}{\sigma_0^2} + \frac{1}{\sigma_y^2}}. \quad (12)$$

335 To solve this Gaussian posterior conditioning task, the RNN response to a constant input $h =$
 336 $yr + (n - M_n)$ must equal the posterior mean along readout vector r , where

$$\kappa_r = \frac{1}{N} \sum_{j=1}^N r_j \phi(x_j). \quad (13)$$

337 Additionally, the amount of chaotic variance Δ_T must equal the posterior variance. Theory for
 338 low-rank RNNs allows us to express κ_r and Δ_T in terms of each other through a solvable system of
 339 nonlinear equations (see Section B.2.4) [26]. This theory facilitates the mathematical formalization
 340 of task execution into an emergent property, where the emergent property statistics of the RNN
 341 activity are κ_r and Δ_T , and the emergent property values are the ground truth posterior mean
 342 μ_{post} and variance σ_{post}^2 :

$$\mathbb{E} \begin{bmatrix} \kappa_r \\ \Delta_T \\ (\kappa_r - \mu_{post})^2 \\ (\Delta_T^2 - \sigma_{post}^2)^2 \end{bmatrix} = \begin{bmatrix} \mu_{post} \\ \sigma_{post}^2 \\ 0.1 \\ 0.1 \end{bmatrix}. \quad (14)$$

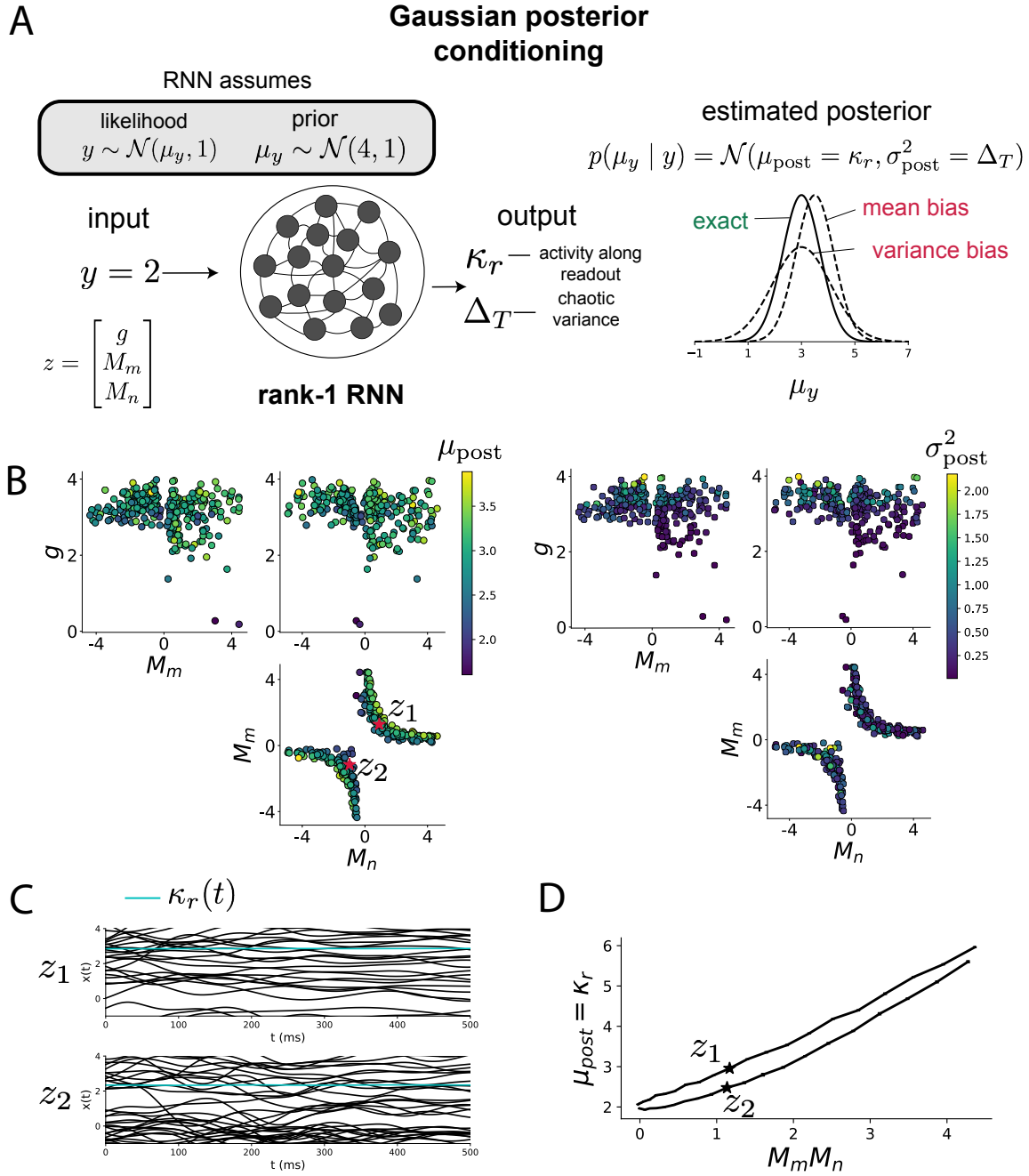


Figure 5: Sources of error in an RNN solving a simple task. A. (left) A rank-1 RNN executing a Gaussian posterior conditioning computation on μ_y . (right) Error in this computation can come from over- or underestimating the posterior mean or variance. B. EPI distribution of rank-1 RNNs executing Gaussian posterior conditioning. Samples are colored by (left) posterior mean $\mu_{\text{post}} = \kappa_r$ and (right) posterior variance $\sigma_{\text{post}}^2 = \Delta_T$. C. Finite-size network simulations of 2,000 neurons with parameters z_1 and z_2 sampled from the inferred distribution. Activity along readout κ_r (cyan) is stable despite chaotic fluctuations. D. The posterior mean computed by RNNs parameterized by z_1 and z_2 perturbed in the dimension of the product of M_m and M_n . Means and standard errors are shown across 10 realizations of 2,000-neuron networks.

343 We chose a substantial amount of variance in these emergent property statistics, so that the inferred
 344 distribution resulted in RNNs with a variety of errors in their solutions to the gaussian posterior
 345 conditioning problem.

346 EPI was used to learn distributions of RNN connectivity properties $z = [g, M_m, M_n]$ executing
 347 Gaussian posterior conditioning given an input of $y = 2$, where the true posterior is $\mu_{\text{post}} = 3$ and
 348 $\sigma_{\text{post}} = 0.5$ (Fig. 5A). We examined the nature of the over- and under-estimation of the posterior
 349 means (Fig. 5B left) and variances (Fig. 5B right) in the inferred distributions (300 samples).
 350 The symmetry in the M_m - M_n plane, suggests a degeneracy in the product of M_m and M_n (Fig.
 351 5B). Indeed, $M_m M_n$ strongly determines the posterior mean ($r = 0.62, p < 10^{-4}$). Furthermore,
 352 the random strength g strongly determines the chaotic variance ($r = 0.56, p < 10^{-4}$). Neither of
 353 these observations were obvious from what mathematical analysis is available in networks of this
 354 type (see Section B.2.4). While the link between random strength g and chaotic variance Δ_T (and
 355 resultingly posterior variance in this problem) is well-known [3], the distribution admits a novel
 356 hypothesis: the estimation of the posterior mean by the RNN increases with $M_m M_n$.

357 We tested this prediction by taking parameters z_1 and z_2 as representative samples from the positive
 358 and negative M_m - M_n quadrants, respectively. Instead of using the theoretical predictions shown in
 359 Figure 5B, we simulated finite-size realizations of these networks with 2,000 neurons (e.g. Fig. 5C).
 360 We perturbed these parameter choices by $M_m M_n$ clarifying that the posterior mean can be directly
 361 controlled in this way (Fig. 5D; $p < 10^{-4}$), see Section B.2.4). Thus, EPI confers a clear picture
 362 of error in this computation: the product of the low rank vector means M_m and M_n modulates
 363 the estimated posterior mean while the random strength g modulates the estimated posterior
 364 variance. This novel procedure of inference on reduced parameterizations of RNNs conditioned on
 365 the emergent property of task execution is generalizable to other settings modeled in [26] like noisy
 366 integration and context-dependent decision making (Fig. S5).

367 4 Discussion

368 4.1 EPI is a general tool for theoretical neuroscience

369 Biologically realistic models of neural circuits are comprised of complex nonlinear differential equa-
 370 tions, making traditional theoretical analysis and statistical inference intractable. In contrast, EPI
 371 is capable of learning distributions of parameters in such models producing measurable signatures
 372 of computation. We have demonstrated its utility on biological models (STG), intermediate-level

373 models of interacting genetically- and functionally-defined neuron-types (V1, SC), and the most
374 abstract of models (RNNs). We are able to condition both deterministic and stochastic models on
375 low-level emergent properties like spiking frequency of membrane potentials, as well as high-level
376 cognitive function like posterior conditioning. Technically, EPI is tractable when the emergent
377 property statistics are continuously differentiable with respect to the model parameters, which is
378 very often the case; this emphasizes the general applicability of EPI.

379 In this study, we have focused on applying EPI to low dimensional parameter spaces of models
380 with low dimensional dynamical states. These choices were made to present the reader with a
381 series of interpretable conclusions, which is more challenging in high dimensional spaces. In fact,
382 EPI should scale reasonably to high dimensional parameter spaces, as the underlying technology has
383 produced state-of-the-art performance on high-dimensional tasks such as texture generation [20]. Of
384 course, increasing the dimensionality of the dynamical state of the model makes optimization more
385 expensive, and there is a practical limit there as with any machine learning approach. Although,
386 theoretical approaches (e.g. [26]) can be used to reason about the wholistic activity of such high
387 dimensional systems by introducing some degree of additional structure into the model.

388 There are additional technical considerations when assessing the suitability of EPI for a particu-
389 lar modeling question. First and foremost, as in any optimization problem, the defined emergent
390 property should always be appropriately conditioned (constraints should not have wildly different
391 units). Furthermore, if the program is underconstrained (not enough constraints), the distribution
392 grows (in entropy) unstably unless mapped to a finite support. If overconstrained, there is no pa-
393 rameter set producing the emergent property, and EPI optimization will fail (appropriately). Next,
394 one should consider the computational cost of the gradient calculations. In the best circumstance,
395 there is a simple, closed form expression (e.g. Section B.1.1) for the emergent property statistic
396 given the model parameters. On the other end of the spectrum, many forward simulation iterations
397 may be required before a high quality measurement of the emergent property statistic is available
398 (e.g. Section B.2.1). In such cases, optimization will be expensive.

399 **4.2 Novel hypotheses from EPI**

400 In neuroscience, machine learning has primarily been used to revealed structure in large-scale neural
401 datasets [51, 52, 53, 54, 55, 56] (see review, [15]). Such careful inference procedures are developed
402 for these statistical models allowing precise, quantitative reasoning, which clarifies the way data
403 informs knowledge of the model parameters. However, these inferable statistical models lack re-

404 semblance to the underlying biology, making it unclear how to go from the structure revealed by
405 these methods, to the neural mechanisms giving rise to it. In contrast, theoretical neuroscience has
406 focused on careful mechanistic modeling and the production of emergent properties of computation.
407 The careful steps of 1.) model design and 2.) emergent property definition, are followed by 3.)
408 practical inference methods resulting in an opaque characterization of the way model parameters
409 govern computation. In this work, we replaced this opaque procedure of parameter identification
410 in theoretical neuroscience with emergent property inference, opening the door to careful inference
411 in careful models of neural computation.

412 Biologically realistic models of neural circuits often prove formidable to analyze. Two main factors
413 contribute to the difficulty of this endeavor. First, even in simple point-neuron circuit models,
414 the number of parameters scales quadratically with the number of neurons, limiting the analytical
415 dissection of its parameter space. Second, even in low dimensional circuits, the structure of the
416 phase space itself is intricate and each parameter configuration can support multiple steady states
417 [57] or non-trivial dynamics on strange attractors [58].

418 In Section 3.3, we advanced the tractability of low-dimensional neuronal circuit models by showing
419 that EPI offers insights about cell-type specific input-responsivity that cannot be afforded through
420 the available linear analytical methods [24, 44, 45]. By flexibly conditioning this V1 model on
421 different emergent properties, we performed an exploratory analysis of a *model* rather than a
422 dataset, generating a set of testable hypotheses, which were proved out. Furthermore, exploratory
423 analyses can be directed towards formulating hypotheses of a specific form. For example, model
424 parameter dependencies on behavioral performance can be assessed by using EPI to condition on
425 various levels of task accuracy (See Section 3.4). This analysis identified experimentally testable
426 predictions (proved out *in-silico*) of patterns of effective connectivity in SC that should be correlated
427 with increased performance.

428 In our final analysis, we presented a novel procedure for doing statistical inference on interpretable
429 parameterizations of RNNs executing simple tasks. Specifically, we analyzed RNNs solving a pos-
430 terior conditioning problem in the spirit of [59]. This methodology relies on recently extended
431 theory of responses in random neural networks with minimal structure [26]. While we focused on
432 rank-1 RNNs, which were sufficient for solving this task, we can more generally use this approach
433 to analyze rank-2 and greater RNNs. The ability to apply the probabilistic model selection toolkit
434 to such black box models should prove invaluable as their use in neuroscience increases.

435 References

- [1] Larry F Abbott. Theoretical neuroscience rising. *Neuron*, 60(3):489–495, 2008.
- [2] John J Hopfield. Neural networks and physical systems with emergent collective computational abilities. *Proceedings of the national academy of sciences*, 79(8):2554–2558, 1982.
- [3] Haim Sompolinsky, Andrea Crisanti, and Hans-Jurgen Sommers. Chaos in random neural networks. *Physical review letters*, 61(3):259, 1988.
- [4] Misha V Tsodyks, William E Skaggs, Terrence J Sejnowski, and Bruce L McNaughton. Paradoxical effects of external modulation of inhibitory interneurons. *Journal of neuroscience*, 17(11):4382–4388, 1997.
- [5] Kong-Fatt Wong and Xiao-Jing Wang. A recurrent network mechanism of time integration in perceptual decisions. *Journal of Neuroscience*, 26(4):1314–1328, 2006.
- [6] Diederik P Kingma and Max Welling. Auto-encoding variational bayes. *International Conference on Learning Representations*, 2014.
- [7] Danilo Jimenez Rezende, Shakir Mohamed, and Daan Wierstra. Stochastic backpropagation and variational inference in deep latent gaussian models. *International Conference on Machine Learning*, 2014.
- [8] Yuanjun Gao, Evan W Archer, Liam Paninski, and John P Cunningham. Linear dynamical neural population models through nonlinear embeddings. In *Advances in neural information processing systems*, pages 163–171, 2016.
- [9] Yuan Zhao and Il Memming Park. Recursive variational bayesian dual estimation for nonlinear dynamics and non-gaussian observations. *stat*, 1050:27, 2017.
- [10] Gabriel Barello, Adam Charles, and Jonathan Pillow. Sparse-coding variational auto-encoders. *bioRxiv*, page 399246, 2018.
- [11] Chethan Pandarinath, Daniel J O’Shea, Jasmine Collins, Rafal Jozefowicz, Sergey D Stavisky, Jonathan C Kao, Eric M Trautmann, Matthew T Kaufman, Stephen I Ryu, Leigh R Hochberg, et al. Inferring single-trial neural population dynamics using sequential auto-encoders. *Nature methods*, page 1, 2018.

- [12] Alexander B Wiltschko, Matthew J Johnson, Giuliano Iurilli, Ralph E Peterson, Jesse M Katon, Stan L Pashkovski, Victoria E Abraira, Ryan P Adams, and Sandeep Robert Datta. Mapping sub-second structure in mouse behavior. *Neuron*, 88(6):1121–1135, 2015.
- [13] Matthew J Johnson, David K Duvenaud, Alex Wiltschko, Ryan P Adams, and Sandeep R Datta. Composing graphical models with neural networks for structured representations and fast inference. In *Advances in neural information processing systems*, pages 2946–2954, 2016.
- [14] Eleanor Batty, Matthew Whiteway, Shreya Saxena, Dan Biderman, Taiga Abe, Simon Musall, Winthrop Gillis, Jeffrey Markowitz, Anne Churchland, John Cunningham, et al. Behavenet: nonlinear embedding and bayesian neural decoding of behavioral videos. *Advances in Neural Information Processing Systems*, 2019.
- [15] Liam Paninski and John P Cunningham. Neural data science: accelerating the experiment-analysis-theory cycle in large-scale neuroscience. *Current opinion in neurobiology*, 50:232–241, 2018.
- [16] Mark K Transtrum, Benjamin B Machta, Kevin S Brown, Bryan C Daniels, Christopher R Myers, and James P Sethna. Perspective: Sloppiness and emergent theories in physics, biology, and beyond. *The Journal of chemical physics*, 143(1):07B201_1, 2015.
- [17] Danilo Jimenez Rezende and Shakir Mohamed. Variational inference with normalizing flows. *International Conference on Machine Learning*, 2015.
- [18] Laurent Dinh, Jascha Sohl-Dickstein, and Samy Bengio. Density estimation using real nvp. *arXiv preprint arXiv:1605.08803*, 2016.
- [19] George Papamakarios, Theo Pavlakou, and Iain Murray. Masked autoregressive flow for density estimation. In *Advances in Neural Information Processing Systems*, pages 2338–2347, 2017.
- [20] Gabriel Loaiza-Ganem, Yuanjun Gao, and John P Cunningham. Maximum entropy flow networks. *International Conference on Learning Representations*, 2017.
- [21] Dustin Tran, Rajesh Ranganath, and David Blei. Hierarchical implicit models and likelihood-free variational inference. In *Advances in Neural Information Processing Systems*, pages 5523–5533, 2017.
- [22] Mark S Goldman, Jorge Golowasch, Eve Marder, and LF Abbott. Global structure, robustness, and modulation of neuronal models. *Journal of Neuroscience*, 21(14):5229–5238, 2001.

- [491] [23] Gabrielle J Gutierrez, Timothy O’Leary, and Eve Marder. Multiple mechanisms switch an
[492] electrically coupled, synaptically inhibited neuron between competing rhythmic oscillators.
[493] *Neuron*, 77(5):845–858, 2013.
- [494] [24] Ashok Litwin-Kumar, Robert Rosenbaum, and Brent Doiron. Inhibitory stabilization and vi-
[495] sual coding in cortical circuits with multiple interneuron subtypes. *Journal of neurophysiology*,
[496] 115(3):1399–1409, 2016.
- [497] [25] Chunyu A Duan, Marino Pagan, Alex T Piet, Charles D Kopec, Athena Akrami, Alexander J
[498] Riordan, Jeffrey C Erlich, and Carlos D Brody. Collicular circuits for flexible sensorimotor
[499] routing. *bioRxiv*, page 245613, 2018.
- [500] [26] Francesca Mastrogiovanni and Srdjan Ostojic. Linking connectivity, dynamics, and computa-
[501] tions in low-rank recurrent neural networks. *Neuron*, 99(3):609–623, 2018.
- [502] [27] Sean R Bittner, Agostina Palmigiano, Kenneth D Miller, and John P Cunningham. Degener-
[503] ate solution networks for theoretical neuroscience. *Computational and Systems Neuroscience
[504] Meeting (COSYNE), Lisbon, Portugal*, 2019.
- [505] [28] Sean R Bittner, Alex T Piet, Chunyu A Duan, Agostina Palmigiano, Kenneth D Miller,
[506] Carlos D Brody, and John P Cunningham. Examining models in theoretical neuroscience with
[507] degenerate solution networks. *Bernstein Conference 2019, Berlin, Germany*, 2019.
- [508] [29] Marcel Nonnenmacher, Pedro J Goncalves, Giacomo Bassetto, Jan-Matthis Lueckmann, and
[509] Jakob H Macke. Robust statistical inference for simulation-based models in neuroscience. In
[510] *Bernstein Conference 2018, Berlin, Germany*, 2018.
- [511] [30] Deistler Michael, , Pedro J Goncalves, Kaan Oecal, and Jakob H Macke. Statistical inference for
[512] analyzing sloppiness in neuroscience models. In *Bernstein Conference 2019, Berlin, Germany*,
[513] 2019.
- [514] [31] Jan-Matthis Lueckmann, Pedro J Goncalves, Giacomo Bassetto, Kaan Öcal, Marcel Nonnen-
[515] macher, and Jakob H Macke. Flexible statistical inference for mechanistic models of neural
[516] dynamics. In *Advances in Neural Information Processing Systems*, pages 1289–1299, 2017.
- [517] [32] Eve Marder and Vatsala Thirumalai. Cellular, synaptic and network effects of neuromodula-
[518] tion. *Neural Networks*, 15(4-6):479–493, 2002.

- 519 [33] Astrid A Prinz, Dirk Bucher, and Eve Marder. Similar network activity from disparate circuit
520 parameters. *Nature neuroscience*, 7(12):1345, 2004.
- 521 [34] Edwin T Jaynes. Information theory and statistical mechanics. *Physical review*, 106(4):620,
522 1957.
- 523 [35] Gamaleldin F Elsayed and John P Cunningham. Structure in neural population recordings:
524 an expected byproduct of simpler phenomena? *Nature neuroscience*, 20(9):1310, 2017.
- 525 [36] Cristina Savin and Gašper Tkačik. Maximum entropy models as a tool for building precise
526 neural controls. *Current opinion in neurobiology*, 46:120–126, 2017.
- 527 [37] Brendan K Murphy and Kenneth D Miller. Balanced amplification: a new mechanism of
528 selective amplification of neural activity patterns. *Neuron*, 61(4):635–648, 2009.
- 529 [38] Hirofumi Ozeki, Ian M Finn, Evan S Schaffer, Kenneth D Miller, and David Ferster. Inhibitory
530 stabilization of the cortical network underlies visual surround suppression. *Neuron*, 62(4):578–
531 592, 2009.
- 532 [39] Daniel B Rubin, Stephen D Van Hooser, and Kenneth D Miller. The stabilized supralinear
533 network: a unifying circuit motif underlying multi-input integration in sensory cortex. *Neuron*,
534 85(2):402–417, 2015.
- 535 [40] Henry Markram, Maria Toledo-Rodriguez, Yun Wang, Anirudh Gupta, Gilad Silberberg, and
536 Caizhi Wu. Interneurons of the neocortical inhibitory system. *Nature reviews neuroscience*,
537 5(10):793, 2004.
- 538 [41] Bernardo Rudy, Gordon Fishell, SooHyun Lee, and Jens Hjerling-Leffler. Three groups of
539 interneurons account for nearly 100% of neocortical gabaergic neurons. *Developmental neuro-*
540 *biology*, 71(1):45–61, 2011.
- 541 [42] Robin Tremblay, Soohyun Lee, and Bernardo Rudy. GABAergic Interneurons in the Neocortex:
542 From Cellular Properties to Circuits. *Neuron*, 91(2):260–292, 2016.
- 543 [43] Carsten K Pfeffer, Mingshan Xue, Miao He, Z Josh Huang, and Massimo Scanziani. Inhi-
544 bition of inhibition in visual cortex: the logic of connections between molecularly distinct
545 interneurons. *Nature Neuroscience*, 16(8):1068, 2013.

- 546 [44] Luis Carlos Garcia Del Molino, Guangyu Robert Yang, Jorge F. Mejias, and Xiao Jing Wang.
547 Paradoxical response reversal of top- down modulation in cortical circuits with three interneu-
548 ron types. *Elife*, 6:1–15, 2017.
- 549 [45] Guang Chen, Carl Van Vreeswijk, David Hansel, and David Hansel. Mechanisms underlying
550 the response of mouse cortical networks to optogenetic manipulation. 2019.
- 551 [46] (2018) Allen Institute for Brain Science. Layer 4 model of v1. available from:
552 <https://portal.brain-map.org/explore/models/l4-mv1>.
- 553 [47] Yazan N Billeh, Binghuang Cai, Sergey L Gratiy, Kael Dai, Ramakrishnan Iyer, Nathan W
554 Gouwens, Reza Abbasi-Asl, Xiaoxuan Jia, Joshua H Siegle, Shawn R Olsen, et al. Systematic
555 integration of structural and functional data into multi-scale models of mouse primary visual
556 cortex. *bioRxiv*, page 662189, 2019.
- 557 [48] Chunyu A Duan, Jeffrey C Erlich, and Carlos D Brody. Requirement of prefrontal and midbrain
558 regions for rapid executive control of behavior in the rat. *Neuron*, 86(6):1491–1503, 2015.
- 559 [49] Omri Barak. Recurrent neural networks as versatile tools of neuroscience research. *Current*
560 *opinion in neurobiology*, 46:1–6, 2017.
- 561 [50] David Sussillo and Omri Barak. Opening the black box: low-dimensional dynamics in high-
562 dimensional recurrent neural networks. *Neural computation*, 25(3):626–649, 2013.
- 563 [51] Robert E Kass and Valérie Ventura. A spike-train probability model. *Neural computation*,
564 13(8):1713–1720, 2001.
- 565 [52] Emery N Brown, Loren M Frank, Dengda Tang, Michael C Quirk, and Matthew A Wilson.
566 A statistical paradigm for neural spike train decoding applied to position prediction from
567 ensemble firing patterns of rat hippocampal place cells. *Journal of Neuroscience*, 18(18):7411–
568 7425, 1998.
- 569 [53] Liam Paninski. Maximum likelihood estimation of cascade point-process neural encoding
570 models. *Network: Computation in Neural Systems*, 15(4):243–262, 2004.
- 571 [54] M Yu Byron, John P Cunningham, Gopal Santhanam, Stephen I Ryu, Krishna V Shenoy, and
572 Maneesh Sahani. Gaussian-process factor analysis for low-dimensional single-trial analysis
573 of neural population activity. In *Advances in neural information processing systems*, pages
574 1881–1888, 2009.

- 575 [55] Kenneth W Latimer, Jacob L Yates, Miriam LR Meister, Alexander C Huk, and Jonathan W
576 Pillow. Single-trial spike trains in parietal cortex reveal discrete steps during decision-making.
577 *Science*, 349(6244):184–187, 2015.
- 578 [56] Lea Duncker, Gergo Bohner, Julien Boussard, and Maneesh Sahani. Learning interpretable
579 continuous-time models of latent stochastic dynamical systems. *Proceedings of the 36th Inter-*
580 *national Conference on Machine Learning*, 2019.
- 581 [57] Nataliya Kraynyukova and Tatjana Tchumatchenko. Stabilized supralinear network can give
582 rise to bistable, oscillatory, and persistent activity. *Proceedings of the National Academy of*
583 *Sciences*, 115(13):3464–3469, 2018.
- 584 [58] Katherine Morrison, Anda Degeratu, Vladimir Itskov, and Carina Curto. Diversity of emer-
585 gent dynamics in competitive threshold-linear networks: a preliminary report. *arXiv preprint*
586 *arXiv:1605.04463*, 2016.
- 587 [59] Rodrigo Echeveste, Laurence Aitchison, Guillaume Hennequin, and Máté Lengyel. Cortical-like
588 dynamics in recurrent circuits optimized for sampling-based probabilistic inference. *bioRxiv*,
589 page 696088, 2019.
- 590 [60] David M Blei, Alp Kucukelbir, and Jon D McAuliffe. Variational inference: A review for
591 statisticians. *Journal of the American Statistical Association*, 112(518):859–877, 2017.
- 592 [61] Rajesh Ranganath, Sean Gerrish, and David Blei. Black box variational inference. In *Artificial*
593 *Intelligence and Statistics*, pages 814–822, 2014.
- 594 [62] Martin J Wainwright, Michael I Jordan, et al. Graphical models, exponential families, and
595 variational inference. *Foundations and Trends® in Machine Learning*, 1(1–2):1–305, 2008.
- 596 [63] Diederik P Kingma and Jimmy Ba. Adam: A method for stochastic optimization. *International*
597 *Conference on Learning Representations*, 2015.
- 598 [64] Laurent Dinh, Jascha Sohl-Dickstein, and Samy Bengio. Density estimation using real nvp.
599 *Proceedings of the 5th International Conference on Learning Representations*, 2017.
- 600 [65] Nicolas Brunel. Dynamics of sparsely connected networks of excitatory and inhibitory spiking
601 neurons. *Journal of computational neuroscience*, 8(3):183–208, 2000.
- 602 [66] Herbert Jaeger and Harald Haas. Harnessing nonlinearity: Predicting chaotic systems and
603 saving energy in wireless communication. *science*, 304(5667):78–80, 2004.

- 604 [67] David Sussillo and Larry F Abbott. Generating coherent patterns of activity from chaotic
605 neural networks. *Neuron*, 63(4):544–557, 2009.

606 A Acknowledgements

607 This work was funded by NSF Graduate Research Fellowship, DGE-1644869, McKnight Endow-
 608 ment Fund, NIH NINDS 5R01NS100066, Simons Foundation 542963, NSF NeuroNex Award, DBI-
 609 1707398, The Gatsby Charitable Foundation, Simons Collaboration on the Global Brain Postdoc-
 610 toral Fellowship, Chinese Postdoctoral Science Foundation, and International Exchange Program
 611 Fellowship. Helpful conversations were had with Francesca Mastrogiuseppe, Srdjan Ostojic, James
 612 Fitzgerald, Stephen Baccus, Dhruva Raman, Mehrdad Jazayeri, Liam Paninski, and Larry Abbott.

613 B Methods

614 B.1 Emergent property inference (EPI)

615 Emergent property inference (EPI) learns distributions of theoretical model parameters that pro-
 616 duce emergent properties of interest by combining ideas from maximum entropy flow networks
 617 (MEFNs) [20] and likelihood-free variational inference (LFVI) [21]. Consider model parameteri-
 618 zation z and data x which has an intractable likelihood $p(x | z)$ defined by a model simulator of
 619 which samples are available $x \sim p(x | z)$. EPI optimizes a distribution $q_\theta(z)$ (itself parameterized
 620 by θ) of model parameters z to produce an emergent property of interest \mathcal{B} ,

$$\mathcal{B} \triangleq \mathbb{E}_{z \sim q_\theta} [\mathbb{E}_{x \sim p(x|z)} [T(x)]] = \mu. \quad (15)$$

621 Precisely, the emergent property statistics $T(x)$ must equal the emergent property values μ , in
 622 expectation over the EPI distribution of parameters $q_\theta(z)$ and the distribution of simulated activity
 623 $p(x | z)$. This is a viable way to represent emergent properties in theoretical models, as we have
 624 demonstrated in the main text, and enables the EPI optimization.

625 With EPI, we use deep probability distributions to learn flexible approximations to model parameter
 626 distributions $q_\theta(z)$. In deep probability distributions, a simple random variable $w \sim q_0(w)$ is
 627 mapped deterministically via a sequence of deep neural network layers (f_1, \dots, f_l) parameterized by
 628 weights and biases θ to the support of the distribution of interest:

$$z = f_\theta(\omega) = f_l(\dots f_1(w)). \quad (16)$$

629 Given a simulator defined by a theoretical model $x \sim p(x | z)$ and some emergent property of
 630 interest \mathcal{B} , $q_\theta(z)$ is optimized via the neural network parameters θ to find a maximally entropic

631 distribution q_θ^* within the deep variational family \mathcal{Q} producing the emergent property:

$$\begin{aligned} q_\theta^*(z) &= \operatorname{argmax}_{q_\theta \in \mathcal{Q}} H(q_\theta(z)) \\ \text{s.t. } \mathbb{E}_{z \sim q_\theta} [\mathbb{E}_{x \sim p(x|z)} [T(x)]] &= \mu. \end{aligned} \quad (17)$$

632 Since we are optimizing parameters θ of our deep probability distribution with respect to the
 633 entropy $H(q_\theta(z))$, we must take gradients with respect to the log probability density of samples
 634 from the deep probability distribution. Entropy of $q_\theta(z)$ can be expressed as an expectation of
 635 the negative log density of parameter samples z over the randomness in the parameterless initial
 636 distribution q_0 :

$$H(q_\theta(z)) = \int -q_\theta(z) \log(q_\theta(z)) dz = \mathbb{E}_{z \sim q_\theta} [-\log(q_\theta(z))] = \mathbb{E}_{w \sim q_0} [-\log(q_\theta(f_\theta(w)))]. \quad (18)$$

637 Thus, the gradient of the entropy of the deep probability distribution can be estimated as an
 638 average of gradients of the log density of samples z :

$$\nabla_\theta H(q_\theta(z)) = \mathbb{E}_{w \sim q_0} [-\nabla_\theta \log(q_\theta(f_\theta(w)))]. \quad (19)$$

639 In EPI, MEFNs are purposed towards variational learning of model parameter distributions. A
 640 closely related methodology, variational inference, uses optimization to approximate posterior dis-
 641 tributions [60]. Standard methods like stochastic gradient variational Bayes [6] or black box varia-
 642 tional inference [61] simply do not work for inference in theoretical models of neural circuits, since
 643 they require tractable likelihoods $p(x | z)$. Work on likelihood-free variational inference (LFVI) [21],
 644 which like EPI seeks to do inference in models with intractable likelihoods, employs an addtional
 645 deep neural network as a ratio estimator, enabling an estimation of the optimization objective for
 646 variational inference. Like LFVI, EPI can be framed as variational inference (see Section B.1.4).
 647 But, unlike LFVI, EPI uses a single deep network to learn a distribution and is optimized to pro-
 648 duce an emergent property, rather than condition on data points. Optimizing the EPI objective is
 649 a technological challenge, the details of which we elaborate in Section B.1.2. Before going through
 650 those details, we ground this optimization in a toy example.

651 B.1.1 Example: 2D LDS

652 To gain intuition for EPI, consider a two-dimensional linear dynamical system (2D LDS) model
 653 (Fig. S1A):

$$\tau \frac{dx}{dt} = Ax \quad (20)$$

654 with

$$A = \begin{bmatrix} a_1 & a_2 \\ a_3 & a_4 \end{bmatrix}. \quad (21)$$

655 To run EPI with the dynamics matrix elements as the free parameters $z = [a_1, a_2, a_3, a_4]$ (fixing
 656 $\tau = 1$), the emergent property statistics $T(x)$ were chosen to contain the first and second moments
 657 of the oscillatory frequency, $2\pi\text{imag}(\lambda_1)$, and the growth/decay factor, $\text{real}(\lambda_1)$, of the oscillating
 658 system. λ_1 is the eigenvalue of greatest real part when the imaginary component is zero, and
 659 alternatively of positive imaginary component when the eigenvalues are complex conjugate pairs.
 660 To learn the distribution of real entries of A that produce a band of oscillating systems around
 661 1Hz, we formalized this emergent property as $\text{real}(\lambda_1)$ having mean zero with variance 0.25², and
 662 the oscillation frequency $2\pi\text{imag}(\lambda_1)$ having mean $\omega = 1$ Hz with variance (0.1Hz)²:

$$\mathbb{E}[T(x)] \triangleq \mathbb{E} \begin{bmatrix} \text{real}(\lambda_1) \\ \text{imag}(\lambda_1) \\ (\text{real}(\lambda_1) - 0)^2 \\ (\text{imag}(\lambda_1) - 2\pi\omega)^2 \end{bmatrix} = \begin{bmatrix} 0.0 \\ 2\pi\omega \\ 0.25^2 \\ (2\pi 0.1)^2 \end{bmatrix} \triangleq \mu. \quad (22)$$

663

664 Unlike the models we presented in the main text, this model admits an analytical form for the
 665 mean emergent property statistics given parameter z , since the eigenvalues can be calculated using
 666 the quadratic formula:

$$\lambda = \frac{\left(\frac{a_1+a_4}{\tau}\right) \pm \sqrt{\left(\frac{a_1+a_4}{\tau}\right)^2 + 4\left(\frac{a_2a_3-a_1a_4}{\tau}\right)}}{2}. \quad (23)$$

667 Importantly, even though $\mathbb{E}_{x \sim p(x|z)}[T(x)]$ is calculable directly via a closed form function and
 668 does not require simulation, we cannot derive the distribution q_θ^* directly. This fact is due to the
 669 formally hard problem of the backward mapping: finding the natural parameters η from the mean
 670 parameters μ of an exponential family distribution [62]. Instead, we used EPI to approximate this
 671 distribution (Fig. S1B). We used a real-NVP normalizing flow architecture with four masks, two
 672 neural network layers of 15 units per mask, with batch normalization momentum 0.99, mapped
 673 onto a support of $z_i \in [-10, 10]$. (see Section B.1.3).

674 Even this relatively simple system has nontrivial (though intuitively sensible) structure in the
 675 parameter distribution. To validate our method, we analytically derived the contours of the prob-
 676 ability density from the emergent property statistics and values. In the a_1 - a_4 plane, the black
 677 line at $\text{real}(\lambda_1) = \frac{a_1+a_4}{2} = 0$, dotted black line at the standard deviation $\text{real}(\lambda_1) = \frac{a_1+a_4}{2} \pm 0.25$,
 678 and the dotted gray line at twice the standard deviation $\text{real}(\lambda_1) = \frac{a_1+a_4}{2} \pm 0.5$ follow the contour

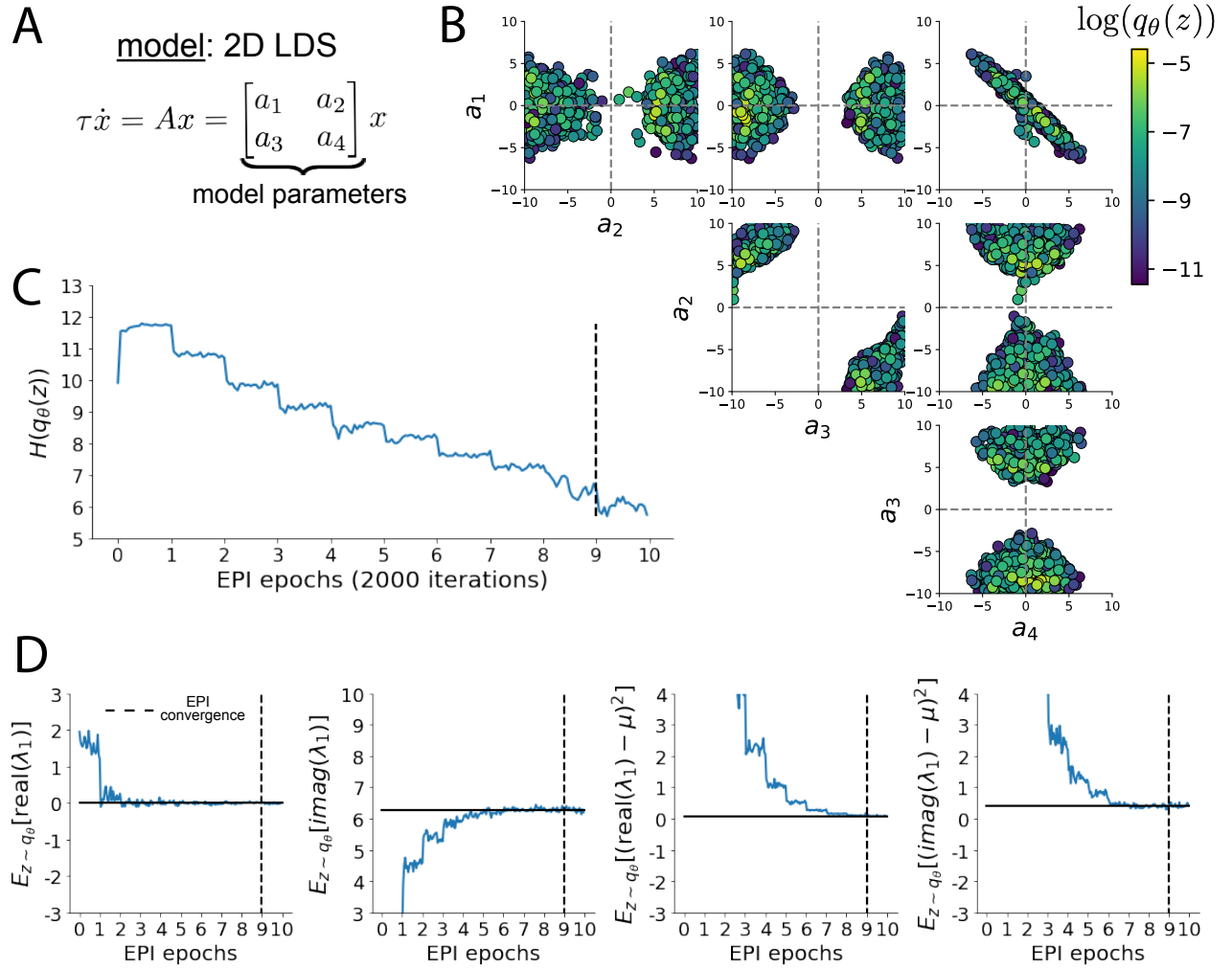


Fig. S1: A. Two-dimensional linear dynamical system model, where real entries of the dynamics matrix A are the parameters. B. The EPI distribution for a two-dimensional linear dynamical system with $\tau = 1$ that produces an average of 1Hz oscillations with some small amount of variance. Dashed lines indicate the parameter axes. C. Entropy throughout the optimization. At the beginning of each augmented Lagrangian epoch (2,000 iterations), the entropy dipped due to the shifted optimization manifold where emergent property constraint satisfaction is increasingly weighted. D. Emergent property moments throughout optimization. At the beginning of each augmented Lagrangian epoch, the emergent property moments adjust closer to their constraints.

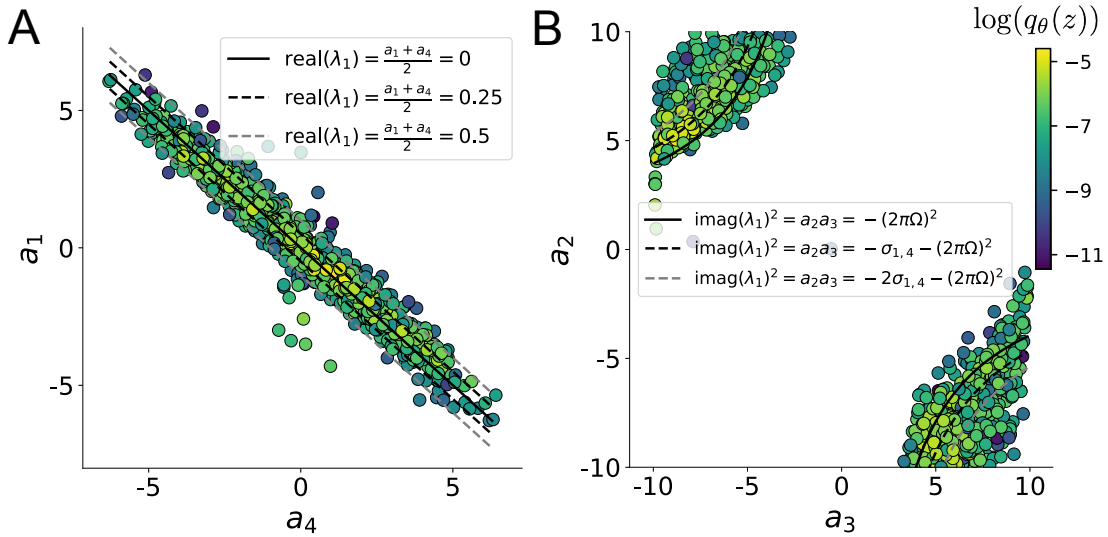


Fig. S2: A. Probability contours in the a_1 - a_4 plane were derived from the relationship to emergent property statistic of growth/decay factor $\text{real}(\lambda_1)$. B. Probability contours in the a_2 - a_3 plane were derived from the emergent property statistic of oscillation frequency $2\pi\text{imag}(\lambda_1)$.

679 of probability density of the samples (Fig. S2A). The distribution precisely reflects the desired
 680 statistical constraints and model degeneracy in the sum of a_1 and a_4 . Intuitively, the parameters
 681 equivalent with respect to emergent property statistic $\text{real}(\lambda_1)$ have similar log densities.

682 To explain the bimodality of the EPI distribution, we examined the imaginary component of λ_1 .

683 When $\text{real}(\lambda_1) = \frac{a_1 + a_4}{2} = 0$, we have

$$\text{imag}(\lambda_1) = \begin{cases} \sqrt{\frac{a_1 a_4 - a_2 a_3}{\tau}}, & \text{if } a_1 a_4 < a_2 a_3 \\ 0 & \text{otherwise} \end{cases}. \quad (24)$$

684 When $\tau = 1$ and $a_1 a_4 > a_2 a_3$ (center of distribution above), we have the following equation for the
 685 other two dimensions:

$$\text{imag}(\lambda_1)^2 = a_1 a_4 - a_2 a_3 \quad (25)$$

686 Since we constrained $\mathbb{E}_{z \sim q_\theta} [\text{imag}(\lambda)] = 2\pi$ (with $\omega = 1$), we can plot contours of the equation
 687 $\text{imag}(\lambda_1)^2 = a_1 a_4 - a_2 a_3 = (2\pi)^2$ for various $a_1 a_4$ (Fig. S2B). With $\sigma_{1,4} = \mathbb{E}_{z \sim q_\theta} (|a_1 a_4 - E_{q_\theta}[a_1 a_4]|)$,
 688 we show the contours as $a_1 a_4 = 0$ (black), $a_1 a_4 = -\sigma_{1,4}$ (black dotted), and $a_1 a_4 = -2\sigma_{1,4}$ (grey
 689 dotted). This validates the curved structure of the inferred distribution learned through EPI. We
 690 took steps in negative standard deviation of $a_1 a_4$ (dotted and gray lines), since there are few positive
 691 values $a_1 a_4$ in the learned distribution. Subtler combinations of model and emergent property will

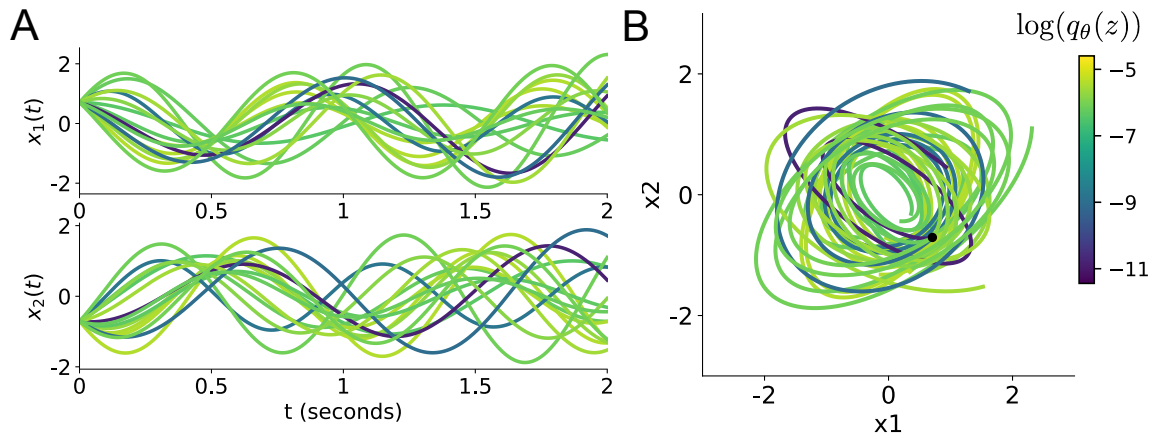


Fig. S3: Sampled dynamical systems $z \sim q_\theta(z)$ and their simulated activity from $x(0) = [\frac{\sqrt{2}}{2}, -\frac{\sqrt{2}}{2}]$ colored by log probability. A. Each dimension of the simulated trajectories throughout time. B The simulated trajectories in phase space.

692 have more complexity, further motivating the use of EPI for understanding these systems. As we
 693 expect, the distribution results in samples of two-dimensional linear systems oscillating near 1Hz
 694 (Fig. S3).

695 **B.1.2 Augmented Lagrangian optimization**

696 To optimize $q_\theta(z)$ in Equation 17, the constrained optimization is executed using the augmented
 697 Lagrangian method. The following objective is minimized:

$$L(\theta; \eta, c) = -H(q_\theta) + \eta^\top R(\theta) + \frac{c}{2} \|R(\theta)\|^2 \quad (26)$$

698 where $R(\theta) = \mathbb{E}_{z \sim q_\theta} [\mathbb{E}_{x \sim p(x|z)} [T(x) - \mu]]$, $\eta \in \mathbb{R}^m$ are the Lagrange multipliers where $m = |\mu| = |T(x)|$, and c is the penalty coefficient. These Lagrange multipliers are closely related to the natural
 699 parameters of exponential families (see Section B.1.4). Deep neural network weights and biases θ of
 700 the deep probability distribution are optimized according to Equation 26 using the Adam optimizer
 701 with its standard parameterization [63]. η is initialized to the zero vector and adapted following
 702 each augmented Lagrangian epoch, which is a period of optimization with fixed (η, c) for a given
 703 number of stochastic optimization iterations. A low value of c is used initially, and conditionally
 704 increased after each epoch based on constraint error reduction. For example, the initial value of
 705 c was $c_0 = 10^{-3}$ during EPI with the oscillating 2D LDS (Fig. S1C). The penalty coefficient is
 706 updated based on the result of a hypothesis test regarding the reduction in constraint violation. The
 707

708 p-value of $\mathbb{E}[|R(\theta_{k+1})|] > \gamma \mathbb{E}[|R(\theta_k)|]$ is computed, and c_{k+1} is updated to βc_k with probability
 709 $1 - p$. The other update rule is $\eta_{k+1} = \eta_k + c_k \frac{1}{n} \sum_{i=1}^n (T(x^{(i)}) - \mu)$ given a batch size n . Throughout
 710 the study, $\beta = 4.0$, $\gamma = 0.25$, and the batch size was a hyperparameter, which varied according to
 711 the application of EPI.

712 The intention is that c and η start at values encouraging entropic growth early in optimization.
 713 With each training epoch in which the update rule for c is invoked by unsatisfactory constraint
 714 error reduction, the constraint satisfaction terms are increasingly weighted, resulting in a decreased
 715 entropy. This encourages the discovery of suitable regions of parameter space, and the subsequent
 716 refinement of the distribution to produce the emergent property. In the oscillating 2D LDS example,
 717 each augmented Lagrangian epoch ran for 2,000 iterations (Fig. S1C-D). Notice the initial entropic
 718 growth, and subsequent reduction upon each update of η and c . The momentum parameters of the
 719 Adam optimizer were reset at the end of each augmented Lagrangian epoch.

720 Rather than starting optimization from some θ drawn from a randomized distribution, we found
 721 that initializing $q_\theta(z)$ to approximate an isotropic Gaussian distribution conferred more stable, con-
 722 sistent optimization. The parameters of the Gaussian initialization were chosen on an applica-
 723 tion-specific basis. Throughout the study, we chose isotropic Gaussian initializations with mean μ_{init} at
 724 the center of the distribution support and some standard deviation σ_{init} , except for one case, where
 725 an initialization informed by random search was used (see Section B.2.2).

726 To assess whether EPI distribution $q_\theta(z)$ produces the emergent property, we defined a hypothesis
 727 testing convergence criteria. The algorithm has converged when a null hypothesis test of constraint
 728 violations $R(\theta)_i$ being zero is accepted for all constraints $i \in \{1, \dots, m\}$ at a significance threshold
 729 $\alpha = 0.05$. This significance threshold is adjusted through Bonferroni correction according to the
 730 number of constraints m . The p-values for each constraint are calculated according to a two-tailed
 731 nonparametric test, where 200 estimations of the sample mean $R(\theta)^i$ are made from k resamplings
 732 of z from a finite sample of size n taken at the end of the augmented Lagrangian epoch. k is
 733 determined by a fraction of the batch size ν , which varies according to the application. In the
 734 linear two-dimensional system example, we used a batch size of $n = 1000$ and set $\nu = 0.1$ resulting
 735 in convergence after the ninth epoch of optimization. (Fig. S1C-D black dotted line).

736 **B.1.3 Normalizing flows**

737 Deep probability models typically consist of several layers of fully connected neural networks.
 738 When each neural network layer is restricted to be a bijective function, the sample density can be
 739 calculated using the change of variables formula at each layer of the network. For $z' = f(z)$,

$$q(z') = q(f^{-1}(z')) \left| \det \frac{\partial f^{-1}(z')}{\partial z'} \right| = q(z) \left| \det \frac{\partial f(z)}{\partial z} \right|^{-1}. \quad (27)$$

740 However, this computation has cubic complexity in dimensionality for fully connected layers. By
 741 restricting our layers to normalizing flows [17] – bijective functions with fast log determinant Ja-
 742 cobian computations, we can tractably optimize deep generative models with objectives that are a
 743 function of sample density, like entropy. Most of our analyses use either a planar flow [17] or real
 744 NVP [64], which have proven effective in our architecture searches. Planar flow architectures are
 745 specified by the number of planar bijection layers used, while real NVP architectures are specified
 746 by the number of masks, neural network layers per mask, units per layer, and batch normalization
 747 momentum parameter.

748 **B.1.4 Emergent property inference as variational inference in an exponential family**

749 Now that we have fully described the EPI method, we consider its broader contextualization as a
 750 statistical method and its relation to Bayesian inference. In Bayesian inference a prior belief about
 751 model parameters z is formalized into a prior distribution $p(z)$, and the statistical model capturing
 752 the effect of z on observed data points x is formalized in the likelihood distribution $p(x | z)$. In
 753 Bayesian inference, we obtain a posterior distribution $p(z | x)$, which captures how the data inform
 754 our knowledge of model parameters using Bayes’ rule:

$$p(z | x) = \frac{p(x | z)p(z)}{p(x)}. \quad (28)$$

755 The posterior distribution is analytically available when the prior is conjugate with the likelihood.
 756 However, conjugacy is rare in practice, and alternative methods, such as variational inference [60],
 757 are utilized.
 758 As we compare EPI to variational inference, it is important to consider that EPI is a maximum
 759 entropy method, and that maximum entropy methods have a fundamental relationship with expo-

760 nential family distributions. A maximum entropy distribution of form:

$$\begin{aligned} p^*(z) &= \operatorname{argmax}_{p \in \mathcal{P}} H(p(z)) \\ \text{s.t. } \mathbb{E}_{z \sim p}[T(z)] &= \mu. \end{aligned} \quad (29)$$

761 will have probability density in the exponential family:

$$p^*(z) \propto \exp(\eta^\top T(z)). \quad (30)$$

762 The mappings between the mean parameterization μ and the natural parameterization η are for-
763 mally hard to identify [62].

764 Now, consider the goal of doing variational inference with an exponential family posterior dis-
765 tribution $p(z | x)$. We use the following abbreviated notation to collect the base measure $b(z)$
766 and sufficient statistics $T(z)$ into $\tilde{T}(z)$ and likewise concatenate a 1 onto the end of the natural
767 parameter $\tilde{\eta}(x)$. The log normalizing constant $A(\eta(x))$ remains unchanged:

$$\begin{aligned} p(z | x) &= b(z) \exp\left(\eta(x)^\top T(z) - A(\eta(x))\right) = \exp\left(\begin{bmatrix} \eta(x) \\ 1 \end{bmatrix}^\top \begin{bmatrix} T(z) \\ b(z) \end{bmatrix} - A(\eta(x))\right) \\ &= \exp\left(\tilde{\eta}(x)^\top \tilde{T}(z) - A(\eta(x))\right) \end{aligned} \quad (31)$$

768 Variational inference with an exponential family posterior distribution uses optimization to mini-
769 mize the following divergence [60]:

$$q_\theta^* = \operatorname{argmin}_{q_\theta \in Q} KL(q_\theta || p(z | x)). \quad (32)$$

770 $q_\theta(z)$ is the variational approximation to the posterior with variational parameters θ . We can write
771 this KL divergence in terms of entropy of the variational approximation:

$$KL(q_\theta || p(z | x)) = \mathbb{E}_{z \sim q_\theta} [\log(q_\theta(z))] - \mathbb{E}_{z \sim q_\theta} [\log(p(z | x))] \quad (33)$$

$$\begin{aligned} &= -H(q_\theta) - \mathbb{E}_{z \sim q_\theta} [\tilde{\eta}(x)^\top \tilde{T}(z) - A(\eta(x))]. \end{aligned} \quad (34)$$

773 As far as the variational optimization is concerned, the log normalizing constant is independent of
774 $q_\theta(z)$, so it can be dropped

$$\operatorname{argmin}_{q_\theta \in Q} KL(q_\theta || p(z | x)) = \operatorname{argmin}_{q_\theta \in Q} -H(q_\theta) - \mathbb{E}_{z \sim q_\theta} [\tilde{\eta}(x)^\top \tilde{T}(z)]. \quad (35)$$

775 Further, we can write the objective in terms of the first moment of the sufficient statistics $\mu =$
776 $\mathbb{E}_{z \sim p(z|x)} [T(z)]$:

$$= \operatorname{argmin}_{q_\theta \in Q} -H(q_\theta) - \mathbb{E}_{z \sim q_\theta} [\tilde{\eta}(x)^\top (\tilde{T}(z) - \mu)] + \tilde{\eta}(x)^\top \mu, \quad (36)$$

777 which simplifies to

$$= \underset{q_\theta \in Q}{\operatorname{argmin}} -H(q_\theta) - \mathbb{E}_{z \sim q_\theta} \left[\tilde{\eta}(x)^\top (\tilde{T}(z) - \mu) \right]. \quad (37)$$

778 .

779 In comparison, in emergent property inference (EPI), we solve the following problem:

$$q_\theta^*(z) = \underset{q_\theta \in Q}{\operatorname{argmax}} H(q_\theta(z)), \text{ s.t. } \mathbb{E}_{z \sim q_\theta} [\mathbb{E}_{x \sim p(x|z)} [T(x)]] = \mu. \quad (38)$$

780 The Lagrangian objective (without augmentation) is

$$q_\theta^* = \underset{q_\theta \in Q}{\operatorname{argmin}} -H(q_\theta) + \eta_{\text{opt}}^\top \left(\mathbb{E}_{z \sim q_\theta} [\tilde{T}(z)] - \mu \right). \quad (39)$$

781 Thus, as the optimization proceeds, η_{opt}^\top should converge to the natural parameter $\tilde{\eta}(x)$ through
782 its adaptations in each epoch (see Section B.1.2).

783 We have shown that there is indeed a clear relationship between Bayesian inference and EPI.
784 Specifically, EPI is executing variational inference in an exponential family posterior, whose suffi-
785 cient statistics are the emergent property statistics and mean parameterization are the emergent
786 property values. However, in EPI we have not specified a prior distribution, or collected data,
787 which can inform us about model parameters. Instead we have a mathematical specification of
788 an emergent property, which the model must produce, and a maximum entropy selection prin-
789 ciple. Accordingly, we replace the notation of $p(z | x)$ with $p(z | \mathcal{B})$ conceptualizing an inferred
790 distribution that obeys emergent property \mathcal{B} (see Section B.1).

791 B.2 Theoretical models

792 In this study, we used emergent property inference to examine several models relevant to theoretical
793 neuroscience. Here, we provide the details of each model and the related analyses.

794 B.2.1 Stomatogastric ganglion

795 We analyze how the parameters $z = [g_{\text{el}}, g_{\text{synA}}]$ govern the emergent phenomena of network syncing
796 in a model of the stomatogastric ganglion (STG) [23] shown in Figure 1A with activity $x =$
797 $[x_{\text{f1}}, x_{\text{f2}}, x_{\text{hub}}, x_{\text{s1}}, x_{\text{s2}}]$, using the same hyperparameter choices as Gutierrez et al. Each neuron's
798 membrane potential $x_\alpha(t)$ for $\alpha \in \{\text{f1}, \text{f2}, \text{hub}, \text{s1}, \text{s2}\}$ is the solution of the following differential
799 equation:

$$C_m \frac{dx_\alpha}{dt} = -[h_{\text{leak}}(x; z) + h_{Ca}(x; z) + h_K(x; z) + h_{hyp}(x; z) + h_{elec}(x; z) + h_{syn}(x; z)]. \quad (40)$$

800 The membrane potential of each neuron is affected by the leak, calcium, potassium, hyperpolariza-
 801 tion, electrical and synaptic currents, respectively, which are functions of all membrane potentials
 802 and the conductance parameters z . The capacitance of the cell membrane was set to $C_m = 1nF$.
 803 Specifically, the currents are the difference in the neuron's membrane potential and that current
 804 type's reversal potential multiplied by a conductance:

$$h_{leak}(x; z) = g_{leak}(x_\alpha - V_{leak}) \quad (41)$$

$$h_{elec}(x; z) = g_{el}(x_\alpha^{post} - x_\alpha^{pre}) \quad (42)$$

$$h_{syn}(x; z) = g_{syn}S_\infty^{pre}(x_\alpha^{post} - V_{syn}) \quad (43)$$

$$h_{Ca}(x; z) = g_{Ca}M_\infty(x_\alpha - V_{Ca}) \quad (44)$$

$$h_K(x; z) = g_KN(x_\alpha - V_K) \quad (45)$$

$$h_{hyp}(x; z) = g_hH(x_\alpha - V_{hyp}). \quad (46)$$

810 The reversal potentials were set to $V_{leak} = -40mV$, $V_{Ca} = 100mV$, $V_K = -80mV$, $V_{hyp} = -20mV$,
 811 and $V_{syn} = -75mV$. The other conductance parameters were fixed to $g_{leak} = 1 \times 10^{-4}\mu S$, g_{Ca} ,
 812 g_K , and g_{hyp} had different values based on fast, intermediate (hub) or slow neuron. The fast
 813 conductances had values $g_{Ca} = 1.9 \times 10^{-2}$, $g_K = 3.9 \times 10^{-2}$, and $g_{hyp} = 2.5 \times 10^{-2}$. The intermediate
 814 conductances had values $g_{Ca} = 1.7 \times 10^{-2}$, $g_K = 1.9 \times 10^{-2}$, and $g_{hyp} = 8.0 \times 10^{-3}$. Finally, the
 815 slow conductances had values $g_{Ca} = 8.5 \times 10^{-3}$, $g_K = 1.5 \times 10^{-2}$, and $g_{hyp} = 1.0 \times 10^{-2}$.

816 Furthermore, the Calcium, Potassium, and hyperpolarization channels have time-dependent gating
 817 dynamics dependent on steady-state gating variables M_∞ , N_∞ and H_∞ , respectively:

$$M_\infty = 0.5 \left(1 + \tanh \left(\frac{x_\alpha - v_1}{v_2} \right) \right) \quad (47)$$

$$\frac{dN}{dt} = \lambda_N(N_\infty - N) \quad (48)$$

$$N_\infty = 0.5 \left(1 + \tanh \left(\frac{x_\alpha - v_3}{v_4} \right) \right) \quad (49)$$

$$\lambda_N = \phi_N \cosh \left(\frac{x_\alpha - v_3}{2v_4} \right) \quad (50)$$

$$\frac{dH}{dt} = \frac{(H_\infty - H)}{\tau_h} \quad (51)$$

$$H_\infty = \frac{1}{1 + \exp \left(\frac{x_\alpha + v_5}{v_6} \right)} \quad (52)$$

823

$$\tau_h = 272 - \left(\frac{-1499}{1 + \exp\left(\frac{-x_\alpha + v_7}{v_8}\right)} \right). \quad (53)$$

824 where we set $v_1 = 0mV$, $v_2 = 20mV$, $v_3 = 0mV$, $v_4 = 15mV$, $v_5 = 78.3mV$, $v_6 = 10.5mV$,
 825 $v_7 = -42.2mV$, $v_8 = 87.3mV$, $v_9 = 5mV$, and $v_{th} = -25mV$.

826 Finally, there is a synaptic gating variable as well:

$$S_\infty = \frac{1}{1 + \exp\left(\frac{v_{th} - x_\alpha}{v_9}\right)}. \quad (54)$$

827 When the dynamic gating variables are considered, this is actually a 15-dimensional nonlinear
 828 dynamical system.

829 In order to measure the frequency of the hub neuron during EPI, the STG model was simulated
 830 for $T = 200$ time steps of $dt = 25ms$. In EPI, since gradients are taken through the simulation
 831 process, the number of time steps are kept modest if possible. The chosen dt and T were the
 832 most computationally convenient choices yielding accurate frequency measurement. Poor resolution
 833 afforded by the discrete Fourier transform motivated the use of an alternative basis of complex
 834 exponentials to measure spiking frequency. Instead, we used a basis of complex exponentials with
 835 frequencies from 0.0-1.0 Hz at 0.01Hz resolution, $\Phi = [0.0, 0.01, \dots, 1.0]^\top$

836 Another consideration was that the frequency spectra of the neuron membrane potentials had sev-
 837 eral peaks. High-frequency sub-threshold activity obscured the maximum frequency measurement
 838 in the complex exponential basis. Accordingly, subthreshold activity was set to zero, and the
 839 whole signal was low-pass filtered with a moving average window of length 20. The signal was
 840 subsequently mean centered. After this preprocessing, the maximum frequency in the filter bank
 841 accurately reflected the firing frequency.

842 Finally, to differentiate through the maximum frequency identification, we used a sum-of-powers
 843 normalization. Let $\mathcal{X}_\alpha \in \mathcal{C}^{|\Phi|}$ be the complex exponential filter bank dot products with the signal
 844 $x_\alpha \in \mathbb{R}^N$, where $\alpha \in \{f1, f2, \text{hub}, s1, s2\}$. The “frequency identification” vector is

$$v_\alpha = \frac{|\mathcal{X}_\alpha|^\beta}{\sum_{k=1}^N |\mathcal{X}_\alpha(k)|^\beta}. \quad (55)$$

845 The frequency is then calculated as $\omega_\alpha = v_\alpha^\top \Phi$ with $\beta = 100$.

846 Network syncing, like all other emergent properties in this work, are defined by the emergent
 847 property statistics and values. The emergent property statistics are the first and second moments

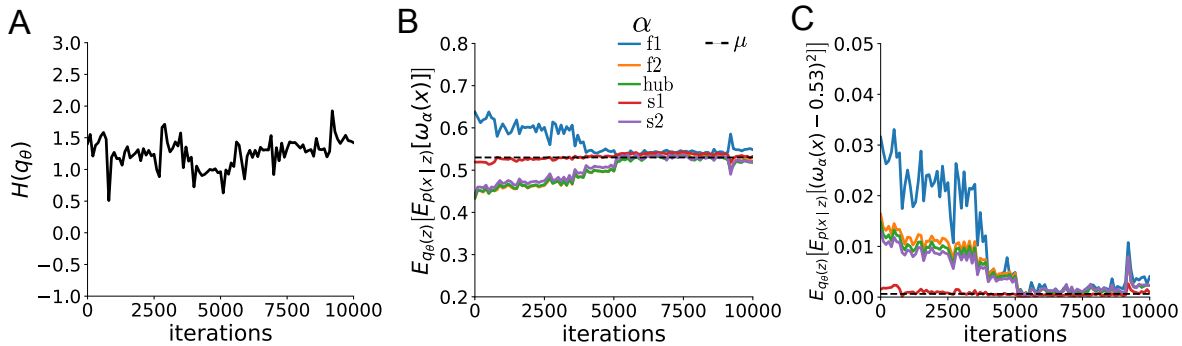


Fig. S4: EPI optimization of the STG model producing network syncing. A. Entropy throughout optimization. B. The first moment emergent property statistics converge to the emergent property values at 10,000 iterations, following the fourth augmented Lagrangian epoch of 2,500 iterations. Since $q_\theta(z)$ failed to produce enough samples yielding $\omega_{f1}(x)$ less than 0.53Hz, the convergence criteria were not satisfied after the third epoch at 7,500 iterations. C. The second moment emergent property statistics converge to the emergent property values.

848 of the firing frequencies. The first moments were set to 0.53Hz, and the second moments were set
 849 to 0.025Hz²:

$$E \begin{bmatrix} \omega_{f1} \\ \omega_{f2} \\ \omega_{\text{hub}} \\ \omega_{s1} \\ \omega_{s2} \\ (\omega_{f1} - 0.53)^2 \\ (\omega_{f2} - 0.53)^2 \\ (\omega_{\text{hub}} - 0.53)^2 \\ (\omega_{s1} - 0.53)^2 \\ (\omega_{s2} - 0.53)^2 \end{bmatrix} = \begin{bmatrix} 0.53 \\ 0.53 \\ 0.53 \\ 0.53 \\ 0.53 \\ 0.025^2 \\ 0.025^2 \\ 0.025^2 \\ 0.025^2 \\ 0.025^2 \end{bmatrix} \quad (56)$$

850 for the EPI distribution shown in Fig. 1B. Throughout optimization, the augmented Lagrangian
 851 parameters η and c , were updated after each epoch of 2,500 iterations (see Section B.1.2). The
 852 optimization converged after four epochs (Fig. S4).

853 For EPI in Fig 2C, we used a real NVP architecture with four masks and two layers of 10 units
 854 per mask, and batch normalization momentum of 0.99 mapped onto a support of $z = [g_{\text{el}}, g_{\text{synA}}] \in$
 855 $[4, 8] \times [0, 4]$. We used an augmented Lagrangian coefficient of $c_0 = 10^2$, a batch size $n = 300$,

856 set $\nu = 0.1$, and initialized $q_\theta(z)$ to produce an isotropic Gaussian with mean $\mu_{\text{init}} = [6, 2]$ with
 857 standard deviation $\sigma_{\text{init}} = 0.5$.

858 We calculated the Hessian at the mode of the inferred EPI distribution. The Hessian of a probability
 859 model is the second order gradient of the log probability density $\log q_\theta(z)$ with respect to the
 860 parameters z : $\frac{\partial^2 \log q_\theta(z)}{\partial z \partial z^\top}$. With EPI, we can examine the Hessian, which is analytically available
 861 throughout distribution, to indicate the dimensions of parameter space that are sensitive (high
 862 magnitude eigenvalue), and which are degenerate (low magnitude eigenvalue) with respect to the
 863 emergent property produced. In Figure 1B, the eigenvectors of the Hessian v_1 and v_2 are shown
 864 evaluated at the mode of the distribution. The length of the arrows is inversely proportional to the
 865 square root of absolute value of their eigenvalues $\lambda_1 = -10.8$ and $\lambda_2 = -2.27$. We quantitatively
 866 measured the sensitivity of the model with respect to network syncing along the eigenvectors of the
 867 Hessian (Fig. 1B, inset). Sensitivity was measured as the slope coefficient of linear regression fit
 868 to network syncing error (the sum of squared differences of each neuron's frequency from 0.53Hz)
 869 as a function of parametric perturbation magnitude (maximum 0.25) away from the mode along
 870 both orientations indicated by the eigenvector with 100 equally spaced samples. The sensitivity
 871 slope coefficient of eigenvector v_1 with respect to network syncing was significant ($\beta = 4.82 \times 10^{-2}$,
 872 $p < 10^{-4}$). In contrast, eigenvector v_2 did not identify a dimension of parameter space significantly
 873 sensitive to network syncing ($\beta = 8.65 \times 10^{-4}$ with $p = .67$). These sensitivities were compared to
 874 all other dimensions of parameter space (100 equally spaced angles from 0 to π), revealing that the
 875 Hessian eigenvectors indeed identified the directions of greatest sensitivity and degeneracy (Fig.
 876 1B, inset). The contours of Figure 1 were calculated as error in $T(x)$ from μ in both the first and
 877 second moment emergent property statistics.

878 **B.2.2 Primary visual cortex**

879 The dynamics of each neural populations average rate $x = [x_E, x_P, x_S, x_V]^\top$ are given by:

$$\tau \frac{dx}{dt} = -x + [Wx + h]_+^n. \quad (57)$$

880 By consolidating information from many experimental datasets, Billeh et al. [47] produce estimates

881 of the synaptic strength (in mV)

$$M = \begin{bmatrix} 0.36 & 0.48 & 0.31 & 0.28 \\ 1.49 & 0.68 & 0.50 & 0.18 \\ 0.86 & 0.42 & 0.15 & 0.32 \\ 1.31 & 0.41 & 0.52 & 0.37 \end{bmatrix} \quad (58)$$

882 and connection probability

$$C = \begin{bmatrix} 0.16 & 0.411 & 0.424 & 0.087 \\ 0.395 & .451 & 0.857 & 0.02 \\ 0.182 & 0.03 & 0.082 & 0.625 \\ 0.105 & 0.22 & 0.77 & 0.028 \end{bmatrix}. \quad (59)$$

883 Multiplying these connection probabilities and synaptic efficacies gives us an effective connectivity

884 matrix:

$$W_{\text{full}} = C \odot M = \begin{bmatrix} 0.16 & 0.411 & 0.424 & 0.087 \\ 0.395 & .451 & 0.857 & 0.02 \\ 0.182 & 0.03 & 0.082 & 0.625 \\ 0.105 & 0.22 & 0.77 & 0.028 \end{bmatrix}. \quad (60)$$

885 Theoretical work on these systems considers a subset of the effective connectivities [24, 44, 45]

$$W = \begin{bmatrix} W_{EE} & W_{EP} & W_{ES} & 0 \\ W_{PE} & W_{PP} & W_{PS} & 0 \\ W_{SE} & 0 & 0 & W_{SV} \\ W_{VE} & W_{VP} & W_{VS} & 0 \end{bmatrix}. \quad (61)$$

886 In coherence with this work, we only keep the entries of W_{full} corresponding to parameters in
887 Equation 61.

888 We look at how this four-dimensional nonlinear dynamical model of V1 responds to different inputs,
889 and compare the predictions of the linear response to the approximate posteriors obtained through
890 EPI. The input to the system is the sum of a baseline input $b = [1, 1, 1, 1]^\top$ and a differential input
891 dh :

$$h = b + dh. \quad (62)$$

892 All simulations of this system had $T = 100$ time points, a time step $dt = 5\text{ms}$, and time constant
893 $\tau = 20\text{ms}$. The system was initialized to a random draw $x(0)_i \sim \mathcal{N}(1, 0.01)$.

894 We can describe the dynamics of this system more generally by

$$\dot{x}_i = -x_i + f(u_i) \quad (63)$$

895 where the input to each neuron is

$$u_i = \sum_j W_{ij} x_j + h_i. \quad (64)$$

896 Let $F_{ij} = \gamma_i \delta(i, j)$, where $\gamma_i = f'(u_i)$. Then, the linear response is

$$\frac{dx_{ss}}{dh} = F(W \frac{dx_{ss}}{dh} + I) \quad (65)$$

897 which is calculable by

$$\frac{dx_{ss}}{dh} = (F^{-1} - W)^{-1}. \quad (66)$$

898 This calculation is used to produce the magenta lines in Figure 2C, which show the linearly predicted
899 inputs that generate a response from two standard deviations (of \mathcal{B}) below and above y .

900 The emergent property we considered was the first and second moments of the change in steady
901 state rate dx_{ss} between the baseline input $h = b$ and $h = b + dh$. We use the following notation to
902 indicate that the emergent property statistics were set to the following values:

$$\mathcal{B}(\alpha, y) \triangleq \mathbb{E} \begin{bmatrix} dx_{\alpha,ss} \\ (dx_{\alpha,ss} - y)^2 \end{bmatrix} = \begin{bmatrix} y \\ 0.01^2 \end{bmatrix}. \quad (67)$$

903 In the final analysis for this model, we sweep the input one neuron at a time away from the mode
904 of each inferred distributions $dh^* = z^* = \text{argmax}_z \log q_\theta(z | \mathcal{B}(\alpha, 0.1))$. The differential responses
905 $\delta x_{\alpha,ss}$ are examined at perturbed inputs $h = b + dh^* + \delta h_\alpha \hat{u}_\alpha$ where \hat{u}_α is a unit vector in the
906 dimension of α and δx is evaluated at 101 equally spaced samples of δh_α from -15 to 15.

907 We measured the linear regression slope between neuron-types of δx and δh to confirm the hy-
908 potheses H1-H3 (H4 is simply observing the nonmonotonicity) and report the p values for tests of
909 non-zero slope.

910 H1: the neuron-type responses are sensitive to their direct inputs. E-population: $\beta = 1.62$,
911 $p < 10^{-4}$ (Fig. 3A black), P-population: $\beta = 1.06$, $p < 10^{-4}$ (Fig. 3B blue), S-population:
912 $\beta = 6.80$, $p < 10^{-4}$ (Fig. 3C red), V-population: $\beta = 6.41$, $p < 10^{-4}$ (Fig. 3D green).
913 H2: the E-population ($\beta = 0$, $p = 1$) and P-populations ($\beta = 0$, $p = 1$) are not affected by
914 δh_V (Fig. 3A green, 3B green);
915 H3: the S-population is not affected by δh_P ($\beta = 0$, $p = 1$) (Fig. 3C blue);

916

917 For each $\mathcal{B}(\alpha, y)$ with $\alpha \in \{E, P, S, V\}$ and $y \in \{0.1, 0.5\}$, we ran EPI using a real NVP architecture
 918 of four masks layers with two hidden layers of 10 units, mapped to a support of $z_i \in [-5, 5]$ with
 919 no batch normalization. We used an augmented Lagrangian coefficient of $c_0 = 10^5$, a batch size
 920 $n = 1000$, set $\nu = 0.5$. The EPI distributions shown in Fig. 2 are the converged distributions with
 921 maximum entropy across random seeds.

922 We set the parameters of the Gaussian initialization μ_{init} and Σ_{init} to the mean and covariance of
 923 random samples $z^{(i)} \sim \mathcal{U}(-5, 5)$ that produced emergent property statistic $dx_{\alpha,ss}$ within a bound
 924 ϵ of the emergent property value y . $\epsilon = 0.01$ was set to be one standard deviation of the emergent
 925 property value according to the emergent property value 0.01^2 of the variance emergent property
 926 statistic.

927 B.2.3 Superior colliculus

928 In the model of Duan et al [25], there are four total units: two in each hemisphere corresponding to
 929 the Pro/Contra and Anti/Ipsi populations. They are denoted as left Pro (LP), left Anti (LA), right
 930 Pro (RP) and right Anti (RA). Each unit has an activity (x_α) and internal variable (u_α) related
 931 by

$$x_\alpha = \left(\frac{1}{2} \tanh \left(\frac{u_\alpha - \epsilon}{\zeta} \right) + \frac{1}{2} \right) \quad (68)$$

932 where $\alpha \in \{LP, LA, RA, RP\}$ $\epsilon = 0.05$ and $\zeta = 0.5$ control the position and shape of the nonlin-
 933 earity, respectively.

934 We order the elements of x and u in the following manner

$$x = \begin{bmatrix} x_{LP} \\ x_{LA} \\ x_{RP} \\ x_{RA} \end{bmatrix} \quad u = \begin{bmatrix} u_{LP} \\ u_{LA} \\ u_{RP} \\ u_{RA} \end{bmatrix}. \quad (69)$$

935 The internal variables follow dynamics:

$$\tau \frac{du}{dt} = -u + Wx + h + \sigma dB \quad (70)$$

936 with time constant $\tau = 0.09s$ and Gaussian noise σdB controlled by the magnitude of $\sigma = 1.0$. The
 937 weight matrix has 8 parameters sW_P , sW_A , vW_{PA} , vW_{AP} , hW_P , hW_A , dW_{PA} , and dW_{AP} (Fig.

938 4B):

$$W = \begin{bmatrix} sW_P & vW_{PA} & hW_P & dW_{PA} \\ vW_{AP} & sW_A & dW_{AP} & hW_A \\ hW_P & dW_{PA} & sW_P & vW_{PA} \\ dW_{AP} & hW_A & vW_{AP} & sW_A \end{bmatrix}. \quad (71)$$

939 The system receives five inputs throughout each trial, which has a total length of 1.8s.

$$h = h_{\text{rule}} + h_{\text{choice-period}} + h_{\text{light}}. \quad (72)$$

940 There are rule-based inputs depending on the condition,

$$h_{P,\text{rule}}(t) = \begin{cases} I_{P,\text{rule}}[1, 0, 1, 0]^\top, & \text{if } t \leq 1.2s \\ 0, & \text{otherwise} \end{cases} \quad (73)$$

941

$$h_{A,\text{rule}}(t) = \begin{cases} I_{A,\text{rule}}[0, 1, 0, 1]^\top, & \text{if } t \leq 1.2s \\ 0, & \text{otherwise} \end{cases} \quad (74)$$

942 a choice-period input,

$$h_{\text{choice}}(t) = \begin{cases} I_{\text{choice}}[1, 1, 1, 1]^\top, & \text{if } t > 1.2s \\ 0, & \text{otherwise} \end{cases} \quad (75)$$

943 and an input to the right or left-side depending on where the light stimulus is delivered.

$$h_{\text{light}}(t) = \begin{cases} I_{\text{light}}[1, 1, 0, 0]^\top, & \text{if } t > 1.2s \text{ and Left} \\ I_{\text{light}}[0, 0, 1, 1]^\top, & \text{if } t > 1.2s \text{ and Right} \\ 0, & t \leq 1.2s \end{cases}. \quad (76)$$

944 The input parameterization was fixed to $I_{P,\text{rule}} = 10$, $I_{A,\text{rule}} = 10$, $I_{\text{choice}} = 2$, and $I_{\text{light}} = 1$.

945 To produce an accuracy rate of p_{LP} in the Left, Pro condition, let \hat{p}_i be the empirical average

946 steady state response (final x_{LP} at end of task) over M=500 Gaussian noise draws for a given SC

947 model parameterization z_i :

$$\hat{p}_i = \mathbb{E}_{\sigma dB} [x_{LP} | s = L, c = P, z = z_i] = \frac{1}{M} \sum_{j=1}^M x_{LP}(s = L, c = P, z = z_i, \sigma dB_j) \quad (77)$$

948 where stimulus $s \in \{L, R\}$, cue $c \in \{P, A\}$, and σdB_j is the Gaussian noise on trial j . As with the

949 V1 model, we only consider steady state responses of x , so x_α is used from here on to denote the

950 steady state activity at the end of the trial. For the first emergent property statistic, the average
 951 over EPI samples (from $q_\theta(z)$) is set to the desired value p_{LP} :

$$\mathbb{E}_{z_i \sim q_\phi} [\mathbb{E}_{\sigma dB} [x_{LP,ss} \mid s = L, c = P, z = z_i]] = \mathbb{E}_{z_i \sim q_\phi} [\hat{p}_i] = p_{LP}. \quad (78)$$

952 For the next emergent property statistic, we ask that the variance of the steady state responses
 953 across Gaussian draws, is the Bernoulli variance for the empirical rate \hat{p}_i :

$$\mathbb{E}_{z \sim q_\phi} [\sigma_{err}^2] = 0 \quad (79)$$

954 where the Bernoulli variance error σ_{err}^2 for the Pro task, left condition is

$$\sigma_{err}^2 = Var_{\sigma dB} [x_{LP} \mid s = L, c = P, z = z_i] - \hat{p}_i(1 - \hat{p}_i). \quad (80)$$

955 We have an additional constraint that the Pro neuron on the opposite hemisphere should have the
 956 opposite value (0 and 1). We can enforce this with another constraint:

$$\mathbb{E}_{z \sim q_\phi} [d_P] = 1, \quad (81)$$

957 where the distance between Pro neuron steady states d_P in the Pro condition is

$$d_P = \mathbb{E}_{\sigma dB} [(x_{LP} - x_{RP})^2 \mid s = L, c = P, z = z_i] \quad (82)$$

958 The emergent property statistics only need to be measured during the Left stimulus condition of
 959 the Pro and Anti tasks, since the network is symmetrically parameterized. In total, the emergent
 960 property of rapid task switching at accuracy level p was defined as

$$\mathcal{B}(p) \triangleq \mathbb{E} \begin{bmatrix} \hat{p}_P \\ \hat{p}_A \\ (\hat{p}_P - p)^2 \\ (\hat{p}_A - p)^2 \\ \sigma_{P,err}^2 \\ \sigma_{A,err}^2 \\ d_P \\ d_A \end{bmatrix} = \begin{bmatrix} p \\ p \\ 0.15^2 \\ 0.15^2 \\ 0 \\ 0 \\ 1 \\ 1 \end{bmatrix}. \quad (83)$$

961 Since the maximum variance of a random variable bounded from 0 to 1 is the Bernoulli variance
 962 $\hat{p}(1 - \hat{p})$, and the maximum squared difference between two variables bounded from 0 to 1 is 1, we
 963 do not need to control the second moment of these test statistics. These variables are dynamical

964 system states and can only exponentially decay (or saturate) to 0 (or 1), so the Bernoulli variance
 965 error and squared difference constraints cannot be satisfied exactly in simulation. This is important
 966 to be mindful of when evaluating the convergence criteria. Instead of using our usual hypothesis
 967 testing criteria for convergence to the emergent property, we set a slack variable threshold only for
 968 these technically infeasible emergent property values to 0.05.

969 Using EPI to learn distributions of dynamical systems producing Bernoulli responses at a given rate
 970 (with small variance around that rate) was more challenging than expected. There is a pathology in
 971 this optimization setup, where the learned distribution of weights is bimodal attributing a fraction
 972 p of the samples to an expansive mode (which always sends x_{LP} to 1), and a fraction $1 - p$ to a
 973 decaying mode (which always sends x_{LP} to 0). This pathology was avoided using an inequality
 974 constraint prohibiting parameter samples that resulted in low variance of responses across noise.

λ	\hat{p}	$q_\theta(z)$	r	p-value
λ_{task}	\hat{p}_P	$q(z \mathcal{B}(60\%))$	1.24×10^{-01}	$p < 10^{-4}$
λ_{task}	\hat{p}_P	$q(z \mathcal{B}(70\%))$	7.56×10^{-01}	$p < 10^{-4}$
λ_{task}	\hat{p}_P	$q(z \mathcal{B}(80\%))$	4.59×10^{-01}	$p < 10^{-4}$
λ_{task}	\hat{p}_P	$q(z \mathcal{B}(90\%))$	3.76×10^{-01}	$p < 10^{-4}$
λ_{task}	\hat{p}_A	$q(z \mathcal{B}(60\%))$	4.80×10^{-02}	$p < .01$
λ_{task}	\hat{p}_A	$q(z \mathcal{B}(70\%))$	2.08×10^{-01}	$p < 10^{-4}$
λ_{task}	\hat{p}_A	$q(z \mathcal{B}(80\%))$	4.84×10^{-01}	$p < 10^{-4}$
λ_{task}	\hat{p}_A	$q(z \mathcal{B}(90\%))$	4.25×10^{-01}	$p < 10^{-4}$
λ_{side}	\hat{p}_P	$q(z \mathcal{B}(50\%))$	-7.57×10^{-02}	$p < 10^{-4}$
λ_{side}	\hat{p}_P	$q(z \mathcal{B}(60\%))$	-6.73×10^{-02}	$p < 10^{-4}$
λ_{side}	\hat{p}_P	$q(z \mathcal{B}(70\%))$	-4.86×10^{-01}	$p < 10^{-4}$
λ_{side}	\hat{p}_P	$q(z \mathcal{B}(80\%))$	-1.43×10^{-01}	$p < 10^{-4}$
λ_{side}	\hat{p}_P	$q(z \mathcal{B}(90\%))$	-1.93×10^{-01}	$p < 10^{-4}$
λ_{side}	\hat{p}_A	$q(z \mathcal{B}(60\%))$	-7.60×10^{-02}	$p < 10^{-4}$
λ_{side}	\hat{p}_A	$q(z \mathcal{B}(70\%))$	-2.73×10^{-01}	$p < 10^{-4}$
λ_{side}	\hat{p}_A	$q(z \mathcal{B}(80\%))$	-2.74×10^{-01}	$p < 10^{-4}$

Table 1: Table of significant correlation values from Fig. 4E.

975 For each accuracy level p , we ran EPI for 10 different random seeds using an architecture of 10
 976 planar flows with a support of $z \in \mathbb{R}^8$. We used an augmented Lagrangian coefficient of $c_0 = 10^2$, a

batch size $n = 300$, and set $\nu = 0.5$, and initialized $q_\theta(z)$ to produce an isotropic Gaussian of zero mean with standard deviation $\sigma_{\text{init}} = 1$. The EPI distributions shown in Fig. 4 are the converged distributions with maximum entropy across random seeds.

We report significant correlations r and their p-values from Figure 4E in Table 1. Correlations were measured from 5,000 samples of $q_\theta(z | \mathcal{B}(p))$ and p-values are reported for one-tailed tests, since we hypothesized a positive correlation between task accuracies p_P or p_A and λ_{task} , and a negative correlation between task accuracies p_P and p_A and λ_{side} .

984 B.2.4 Rank-1 RNN

Extensive research on random fully-connected recurrent neural networks has resulted in foundational theories of their activity [3, 65]. Furthermore, independent research on training these models to perform computations suggests that learning occurs through low-rank perturbations to the connectivity (e.g. [66, 67]). Recent theoretical work extends theory for random neural networks [3] to those with added low-rank structure [26]. In Section 3.5, we used this theory to enable EPI on RNN parameters conditioned on the emergent property of task execution.

Such RNNs have the following dynamics:

$$\frac{dx}{dt} = -x + W\phi(x) + h, \quad (84)$$

where x is network activity, W is the connectivity weight matrix, $\phi(\cdot) = \tanh(\cdot)$ is the input-output function, and h is the input to the system. In a rank-1 RNN (which was sufficiently complex for the Gaussian posterior conditioning task), W is the sum of a random component with strength g and a structured component determined by the outer product of vectors m and n :

$$W = g\chi + \frac{1}{N}mn^\top, \quad (85)$$

where $\chi_{ij} \sim \mathcal{N}(0, \frac{1}{N})$, and the entries of m and n are distributed as $m_i \sim \mathcal{N}(M_m, 1)$ and $n_i \sim \mathcal{N}(M_n, 1)$. For EPI, we consider $z = [g, M_m, M_n]$, which are the parameters governing the connectivity properties of the RNN.

From such a parameterization z , the theory of Mastrogiovanni et al. produces solutions for variables describing the low dimensional response properties of the RNN. These “dynamic mean field” (DMF) variables (e.g. the activity along a vector κ_v , the total variance Δ_0 , structured variance Δ_∞ , and the chaotic variance Δ_T) are derived to be functions of one another and connectivity parameters z . The collection of these derived functions results in a system of equations, whose solution must

1004 be obtained through a nonlinear system of equations solver. The iterative steps of this system
 1005 of equations solver are differentiable, so we take gradients through this solve process. The DMF
 1006 variables provide task-relevant information about the RNN's response to task inputs.

1007 In the Gaussian posterior conditioning example, κ_r and Δ_T are DMF variables used as task-relevant
 1008 emergent property statistics μ_{post} and σ_{post}^2 . Specifically, we solve for the DMF variables κ_r , κ_n ,
 1009 Δ_0 and Δ_∞ , where the readout is nominally chosen to point in the unit orthant $r = [1, \dots, 1]^\top$. The
 1010 consistency equations for these variables in the presence of a constant input $h = yr - (n - M_n)$ can
 1011 be derived following [26]:

$$\begin{aligned} \kappa_r &= G_1(\kappa_r, \kappa_n, \Delta_0, \Delta_\infty) = M_m \kappa_n + y \\ \kappa_n &= G_2(\kappa_r, \kappa_n, \Delta_0, \Delta_\infty) = M_n \langle [\phi_i] \rangle + \langle [\phi'_i] \rangle \\ \frac{\Delta_0^2 - \Delta_\infty^2}{2} &= G_3(\kappa_r, \kappa_n, \Delta_0, \Delta_\infty) = g^2 \left(\int \mathcal{D}z \Phi^2(\kappa_r + \sqrt{\Delta_0} z) - \int \mathcal{D}z \int \mathcal{D}x \Phi(\kappa_r + \sqrt{\Delta_0 - \Delta_\infty} x + \sqrt{\Delta_\infty} z) \right) \\ &\quad + (\kappa_n^2 + 1)(\Delta_0 - \Delta_\infty) \\ \Delta_\infty &= G_4(\kappa_r, \kappa_n, \Delta_0, \Delta_\infty) = g^2 \int \mathcal{D}z \left[\int \mathcal{D}x \phi(\kappa_r + \sqrt{\Delta_0 - \Delta_\infty} x + \sqrt{\Delta_\infty} z) \right]^2 + \kappa_n^2 + 1 \end{aligned} \quad (86)$$

1012 where here z is a gaussian integration variable. We can solve these equations by simulating the
 1013 following Langevin dynamical system to a steady state:

$$\begin{aligned} l(t) &= \frac{\Delta_0(t)^2 - \Delta_\infty(t)^2}{2} \\ \Delta_0(t) &= \sqrt{2l(t) + \Delta_\infty(t)^2} \\ \frac{d\kappa_r(t)}{dt} &= -\kappa_r(t) + G_1(\kappa_r(t), \kappa_n(t), \Delta_0(t), \Delta_\infty(t)) \\ \frac{d\kappa_n(t)}{dt} &= -\kappa_n + G_2(\kappa_r(t), \kappa_n(t), \Delta_0(t), \Delta_\infty(t)) \\ \frac{dl(t)}{dt} &= -l(t) + G_3(\kappa_r(t), \kappa_n(t), \Delta_0(t), \Delta_\infty(t)) \\ \frac{d\Delta_\infty(t)}{dt} &= -\Delta_\infty(t) + G_4(\kappa_r(t), \kappa_n(t), \Delta_0(t), \Delta_\infty(t)) \end{aligned} \quad (87)$$

1014 Then, the chaotic variance, which is necessary for the Gaussian posterior conditioning example, is
 1015 simply calculated via $\Delta_T = \Delta_0 - \Delta_\infty$.

1016 We ran EPI using a real NVP architecture of two masks and two layers per mask with 10 units
 1017 mapped to a support of $z = [g, M_m, M_n] \in [0, 5] \times [-5, 5] \times [-5, 5]$ with no batch normalization.
 1018 We used an augmented Lagrangian coefficient of $c_0 = 1$, a batch size $n = 300$, set $\nu = 0.15$,
 1019 and initialized $q_\theta(z)$ to produce an isotropic Gaussian with mean $\mu_{\text{init}} = [2.5, 0, 0]$ with standard

1020 deviation $\sigma_{\text{init}} = 2.0$. The EPI distribution shown in Fig. 5 is the converged distributions with
1021 maximum entropy across five random seeds.

1022 To examine the effect of product $M_m M_n$ on the posterior mean, μ_{post} we took perturbations in
1023 $M_m M_n$ away from two representative parameters z_1 and z_2 in 21 equally space increments from
1024 -1 to 1. For each perturbation, we sampled 10 2,000-neuron RNNs and measure the calculated
1025 posterior means. In Fig. 5D, we plot the product of $M_m M_n$ in the perturbation versus the average
1026 posterior mean across 10 network realizations with standard error bars. The correlation between
1027 perturbation product $M_m M_n$ and μ_{post} was measured over all simulations. For perturbations away
1028 from z_1 the correlation was 0.995 with $p < 10^{-4}$, and for perturbations away from z_2 the correlation
1029 was 0.983 with $p < 10^{-4}$.

1030 In addition to the Gaussian posterior conditioning example in Section 3.5, we modeled two tasks
1031 from Mastrogiuseppe et al.: noisy detection and context-dependent discrimination. We used the
1032 same theoretical equations and task setups described in their study.

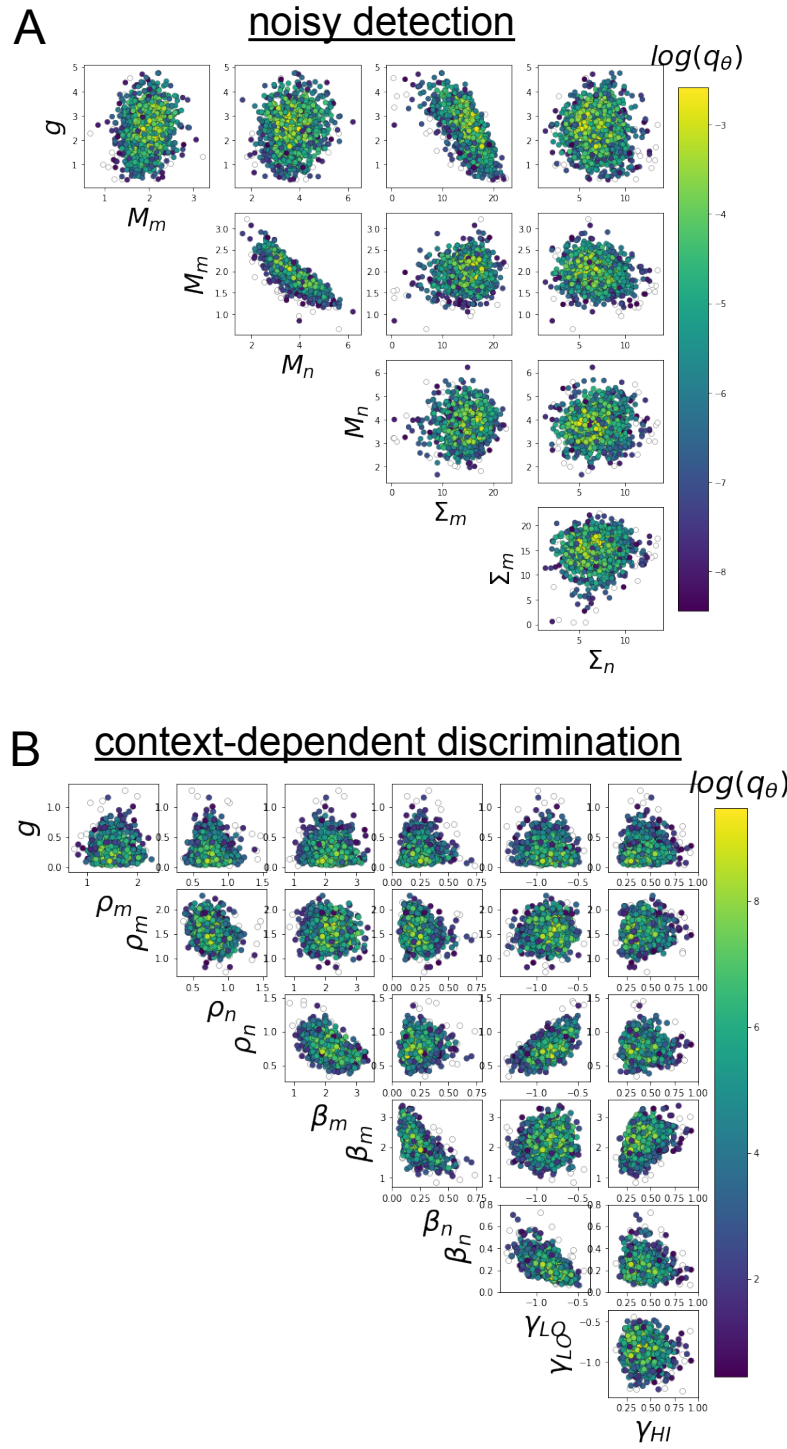


Fig. S5: A. EPI for rank-1 networks doing noisy discrimination. B. EPI for rank-2 networks doing context-dependent discrimination. See [26] for theoretical equations and task description.